Coalescence Dynamics

Eggers,[1] Jens

[1] School of Mathematics, University of Bristol, Fry Building, Woodland Road, Bristol BS8 1UG, UK. email: jens.eggers@bristol.ac.uk

Sprittles,[2] James E.

[2] Mathematics Institute, University of Warwick, Coventry, UK, CV4 7AL; email: J.E.Sprittles@Warwick.ac.uk

Snoeijer,[3] Jacco H.

[3] Physics of Fluids Group, Faculty of Science and Technology, University of Twente, 7500AE Enschede, The Netherlands; email: j.h.snoeijer@utwente.nl

Abstract

The merging of two fluid drops is one of the fundamental topological transitions occurring in free surface flow. Its description has many applications, for example in the chemical industry (emulsions, sprays etc.), in natural flows driving our climate, and for the sintering of materials. After reconnection of two drops, strongly localized surface tension forces drive a singular flow, characterized by a connecting liquid bridge that grows according to scaling laws. We review theory, experiment, and simulation of the coalescence of two spherical drops for different parameters, and in the presence of an outer fluid. We then generalize to other geometries, such as drops spreading on a substrate and in Hele-Shaw flow, and discuss other types of mass transport, apart from viscous flow. Our focus is on times immediately after reconnection, and on the limit of initially undeformed drops at rest relative to one another.
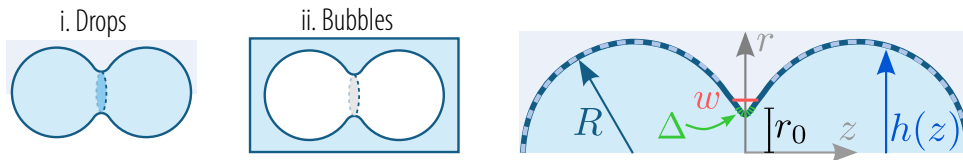
1. Introduction and historical perspective

The coalescence of liquid drops, or other volumes of liquid, is the other fundamental process, complementary to breakup, that takes place in free surface flow (Eggers 1997, Tryggvason et al. 2011, Anthony et al. 2023, Popinet 2018). It is near such singularities where new structures, such as drops, are born, and where rapid motion takes place, which imprints its characteristics on the dynamics. The neighborhood of the places of topological transitions is therefore of special physical and technological interest, and is often characterized by a simplifying self-similar structure. This makes those transitions amenable to analytical mathematical treatment, unusual for highly complex and non-linear free surface flows. Clearly, coalescence processes are of fundamental importance in industrial applications (Kamp et al. 2017), for example in the physics of emulsions (Chesters 1991), for oil recovery (Kavehpour 20015), for inkjet printing (Lohse 2022), for the collision rates in flows containing fluid particles (Liao & Lucas 2010), or for the sintering process (Rahaman 2010), in which a uniform material is created through the merging of individual particles. Models for coalescence have also been applied in biology, rationalizing the merging of cell nucleoli as well as clumps of cells (Pokluda et al. 1997, Flenner et al. 2012, Grosser et al. 2021, Caragine et al. 2018).

Curiously, the driver in both breakup and coalescence is surface tension. In breakup, a sufficiently extended fluid column releases surface energy by reducing its radial extent, which then goes to zero in finite time (Eggers & Villermaux 2008, Eggers & Fontelos 2015, Anthony et al. 2023), but merging of spheres also leads to a reduction of surface area. Once two drops are reconnected by a very small liquid bridge, surface tension will thus induce a very rapid coalescence motion.

The breakup process involves vanishing length and time scales, well separated from those describing smooth motion, leading to universal scaling exponents and self-similar surface profiles, independent of initial conditions and even fluid parameters; thus in breakup the geometry is generated self-consistently and the singularity is encountered during the final stages of breakup. By contrast, in coalescence the motion *starts* in the singular regime and the geometry is imposed by the initial condition. Figure 1 provides an overview of typical coalescence geometries: in contrast to breakup, the resulting coalescence dynamics is not universal, but strongly depends on the imposed geometry e.g. by confinement of the drops (Ryu et al. 2023). Additional complexity comes form the fact that the outer (dispersed) phase also plays a major role in coalescence, even if its viscosity is very small. The reason is that since the outer fluid is confined to a very small gap between the two drops, and lubrication effects come into play.

Coalescence has until recently been considered on a large-scale and qualitative level only (Kamp et al. 2017), the earliest papers being directed toward the conditions under which coalescence takes place in the first instance, for example by Reynolds (1881). The earliest systematic efforts to understand the *dynamics* of coalescence quantitatively, from an experimental (Kuczynski 1949), theoretical (Frenkel 1945, Kuczynski 1949, Hopper 1991), and numerical (Nichols & Mullins 1965) perspective, are related to the (viscous) sintering problem. Other surface-tension-driven transport mechanisms, which dominate at temperatures at which the "drops" are solid, have also been considered widely (Rahaman 2010). The reason for the relative neglect of the initial coalescence process is the tremendous speed of its motion, making experimental (Thoroddsen et al. 2008) and numerical (Sprittles & Shikhmurzaev 2014b, Anthony et al. 2023) approaches very demanding. The very small width of the gap between two spherical drops, in addition, obscures imaging of the liquid bridge, and requires very high numerical resolution.

Spherical or cylindrical (2D) coalescence

i. Drops

ii. Bubbles

Geometrically similar coalescence

iii. Conical drops

iv. Drops on a substrate

v. Liquid lenses
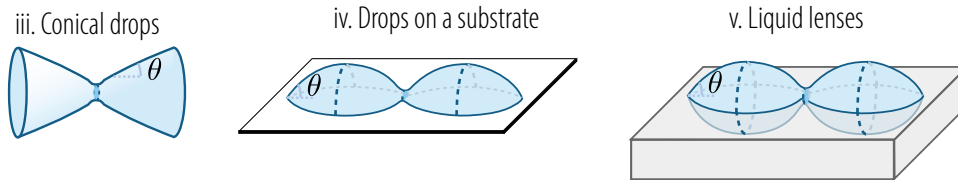
Other geometries or transport mechanisms

vi. Hele-Shaw

vii. Viscoelastic coalescence
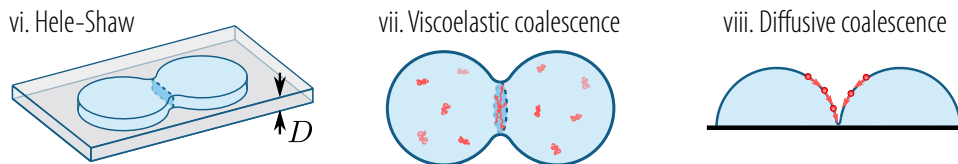
viii. Diffusive coalescence

Figure 1: The dynamics of coalescence is highly dependent on the geometry of the drops at the moment of contact. Spherical coalescence involves drops (i) or bubbles (ii) that are spherical upon the moment of contact. The spherical geometry imposes a hierarchy of scales: drop radius R, bridge radius r_0, bridge width $w = r_0^2/R$, and meniscus curvature $\Delta = r_0^3/R^2$. Geometrically similar coalescence refers to geometrically similar initial conditions, where different directions are related by an angle. Examples are conical drops (iii), drops on a substrate (iv) and liquid lenses (v). The review further covers other geometries and non-Newtonian transport mechanisms, such as drops in a Hele-Shaw cell (vi), viscoelastic drops (vii) and coalescence by diffusive transport (viii).

A complete picture of coalescence would require full understanding of all stages of the process that leads to the complete merging of drops:

1. *Approach.* Two drops first need to be brought together, which in general will be at finite velocity and impact parameter. For example, in a head-on collision of two spherical drops of radius R, travelling at relative speed U, the hypothetical geometrical overlap between the two spheres yields a bridge radius of $r_0 = \sqrt{URt}$, which competes with the singular motion engendered by surface tension, and indicates a non-universal dependence of coalescence dynamics on the impact speed. At small distances, draining of the thin film between the two drops will become important (Davis et al. 1989, Chan et al. 2011, Kamp et al. 2017). As a result, drops will in general be deformed by lubrication forces, in which rarefied gas effects become crucial

(Li 2016, Sprittles 2024).

2. *Reconnection.* Microscopic interactions, through long-ranged intermolecular forces or charge effects, lead to a joining of the two interfaces. This can lead to a "jump to contact", i.e. reconnection before the equilibrium shapes of drops overlap (Beaty & Lister 2023, 2022, Chireux et al. 2018, Quinn et al. 2013, Deblais et al. 2024); the effect of thermal noise may also play a role (Perumanath et al. 2019).

3. *Coalescence.* This is the initial surface-tension-driven merging of two fluid volumes, which is the focus of this review. During this phase the dynamics are confined to a rapid motion of a small liquid bridge connecting the two drops, the size of which is small compared to the drops. As we shall see, in these earliest of stages the centers of mass of the drops move little, since the amount of fluid set in motion by the moving meniscus is small. On account of the locality of the motion, the dynamics is characterized by scaling laws, but with significant exceptions: there can be logarithmic corrections, and profiles do not necessarily exhibit self-similar shapes.

4. *Merging.* The actual merging of the drops, during which the bulk of the original drops interpenetrate to form a larger drop (Ashgriz & Poo 1990, Verdier 2001), and where most of the mass transfer takes place.

This review is dedicated to the *Coalescence* regime that describes the early dynamics after two drops have been joined at a point. Experimentally and numerically, this requires a careful preparation of the initial conditions and very high spatial and temporal resolution. We focus on Newtonian flow of liquid drops and bubbles for the geometries indicated in Fig. 1(i-vi); yet, we will also discuss other transport mechanisms that are relevant e.g. for sintering, as sketched in Fig. 1(vii-viii).

1.1. Time and length scales of Newtonian drop coalescence

$\ell_\nu = \eta^2/(\gamma\rho)$: intrinsic length scale

$t_\nu = \eta^3/(\gamma^2\rho)$: intrinsic time scale

$\mathrm{Oh} = \eta/\sqrt{\rho R \gamma}$: Ohnesorge number, measures the relative importance of viscous to inertial effects.

$\tau_v = \eta R/\gamma$: viscous timescale based on the size of the drop.

$\tau_i = \sqrt{\rho R^3/\gamma}$: inertial timescale based on the size of the drop.

Drops of honey merge very slowly, the surface energy driving the motion being eaten up by viscous friction, while during the rapid coalescence dynamics of water, surface tension is opposed only by inertia, the drops being nearly perfectly inviscid. Using the relevant material parameters for Newtonian drops (surface tension γ, dynamic viscosity η, density ρ), a unique *intrinsic* length scale ℓ_ν, and a time scale t_ν can be constructed (Peregrine et al. 1990, Eggers 1993), at which surface tension, viscosity, and inertia are balanced (see margin note). The size of ℓ_ν relative to the characteristic lengths of the problem determines which regime one is in.

For water $\ell_\nu \approx 14$ nanometer, while for liquid honey ℓ_ν reaches up to several meters. This large variability in ℓ_ν explains why such vastly different dynamics can be observed for millimeter-sized drops. Indeed, introducing the drop size R as an *extrinsic* length scale, the dimensionless ratio $\ell_\nu/R \equiv \mathrm{Oh}^2$ involves the Ohnesorge number, which quantifies the relative importance of viscosity to inertia on the global scale of the drop. The Ohnesorge number can also be written as a ratio of timescales $\mathrm{Oh} = \tau_v/\tau_i$, using the viscous time τ_v and inertial time τ_i (see the margin note). These represent the typical times for the complete merging of two drops in the viscous and inertial regimes, respectively.

In this review we concentrate on the initial stages of coalescence, for which the minimum bridge radius of the fluid neck connecting the two drops $r_0(t) \ll R$ (see Fig. 1). In such an asymptotic limit, and barring logarithmic corrections, one expects the dynamics to have power law form (Eggers & Fontelos 2015), so the asymptotic regimes for the viscous and

inertial bridge dynamics are described by

$$\frac{r_0}{R} \sim \left(\frac{t}{\tau_v}\right)^\alpha, \quad \frac{r_0}{R} \sim \left(\frac{t}{\tau_i}\right)^\beta. \qquad\qquad 1.$$

The exponents α, β are not universal but depend on the coalescence geometry, as we will review in detail (cf. Tables 1 and 2). Special attention will be given to the crossover between viscous and inertial coalescence.

2. Scaling laws: Influence of drop geometry

2.1. Local versus global energy balance

The coalescence of drops is driven by the tendency to reduce surface energy: two drops have a greater surface area than a single merged drop. Refining this argument, Frenkel (1945) put forward the influential idea, both in engineering (Pokluda et al. 1997, Rahaman 2010) and biology (Flenner et al. 2012, Grosser et al. 2021, Caragine et al. 2018), that the rate of coalescence be determined by a balance of the local rate of energy $\dot{E}_\gamma$ freed, with the viscous dissipation inside the drop. The dissipative power can be estimated by $P_\eta \sim \eta \dot{\epsilon}^2 \mathcal{V}$, where $\dot{\epsilon}$ is the typical rate of deformation and $\mathcal{V}$ the characteristic volume that is sheared.

Focusing on the early stages of coalescence, Frenkel (1945) balances $\dot{E}_\gamma = \frac{d}{dt}(\pi \gamma r_0^2)$ with dissipation taking place over the entire drop, i.e. $\mathcal{V} \sim R^3$. This gives the incorrect prediction $r_0 \sim \sqrt{\gamma R t/\eta}$ for spherical drops: in reality the initial motion and thus dissipation is concentrated in a small neck region, with the coalescing drops remaining static.

Yet, in the spirit of Frenkel's calculation, we will use energy balance as a unifying approach to understand the initial coalescence dynamics in a broad class of coalescence geometries (Figure 1), by choosing an appropriate *local* form of the control volume $\mathcal{V}$. In the viscous regime, all the capillary power (surface energy $\gamma \mathcal{A}$ released per unit time; $\gamma \mathcal{L}$ for a 2D object) is dissipated instantaneously by the viscous flow inside the bridge, with $\dot{\epsilon}^2$ and $\mathcal{V}$ to be identified. In the inertial regime, viscous dissipation is subdominant and all the released capillary energy is assumed to be converted into kinetic energy of the moving fluid. Therefore, it natural to invoke the energy balance $E_\gamma = E_{\rm kin} \sim \rho v^2 \mathcal{V}$ (rather than a power balance), where v is the typical velocity inside the bridge. Different coalescence geometries lead to different expressions for $E_\gamma, E_{\rm kin}, P_\eta$, and the resulting bridge dynamics $r_0(t)$ is not at all universal – as discussed in detail below (cf. Tables 1 and 2).

2.2. Spheres

2.2.1. Drops. Assuming a bridge radius r_0, the characteristic width w of the bridge is much smaller and scales as $w = r_0^2/R$ (Figure 1(i)). For a typical millimeter-sized drop, a bridge radius of a micron implies the width to be as small as a nanometer. From the energetic point of view, the width of the bridge can be neglected when computing the released capillary energy, $E_\gamma \sim \gamma r_0^2$. The kinetic energy can be estimated using the velocity $v \sim \dot{r}_0$, which is reached inside the bridge over a volume $\mathcal{V} \sim r_0^2 w \sim r_0^4/R$. The balance of surface and kinetic energies $E_\gamma = \rho v^2 \mathcal{V}$ then gives the inertial scaling $r_0 \sim (\gamma R/\rho)^{1/4} t^{1/2}$. The viscous scaling is more subtle. The dissipated power can be estimated using the rate of deformation $\dot{\epsilon} \sim \dot{r}_0/r_0$. However, owing to the non-local nature of viscous flow, the region over which dissipation occurs extends in all directions, but is cut off at the scale of the two opposing menisci to give $\mathcal{V} \sim r_0^3$. The balance $\dot{E}_\gamma = \eta \dot{\epsilon}^2 \mathcal{V}$ then gives $r_0 \sim \eta t/\gamma$. This scaling argument

Table 1: Scaling laws in the viscous regime: $\dot{E}_\gamma = P_\eta$. Cases for which the drop curvature matters invoke $w = r_0^2/R$ as the bridge width, and $\tau_v = \eta R/\gamma$ as the viscous timescale.

	Capillary power	Viscous dissipation	Bridge scaling	Exponent
	$\frac{d}{dt}(\gamma \mathcal{A})$	$\eta \dot{\epsilon}^2 \mathcal{V}$	$r_0(t)$	α
Spherical drops	$\frac{d}{dt}(\gamma r_0^2)$	$\eta \left(\frac{\dot{r}_0}{r_0}\right)^2 r_0^3$	$\frac{\gamma t}{\eta} \ln(R/r)$	1 (log corr.)
Spherical bubbles	$\frac{d}{dt}(\gamma r_0^2)$	$\eta \left(\frac{\dot{r}_0}{r_0}\right)^2 r_0^2 w$	$\left(\frac{t}{\tau_v}\right)^{1/2} R$	1/2
Hele-Shaw $(D \ll r_0)$	$\frac{d}{dt}(\gamma D r_0)$	$\eta \left(\frac{\dot{r}_0}{D}\right)^2 r_0 D w$	$\left(\frac{t}{\tau_v}\right)^{1/4} \sqrt{RD}$	1/4
Sessile drops (side view, 2D)	$\frac{d}{dt}(\gamma \mathcal{L})$	$\eta \dot{\epsilon}^2 \mathcal{A}$	$h_0(t)$	α
Substrate $(\theta \ll 1)$	$\frac{d}{dt}(\gamma h_0 \theta)$	$\eta \left(\frac{\dot{h}_0/\theta}{h_0}\right)^2 \frac{h_0^2}{\theta}$	$\frac{\gamma t}{\eta} \theta^4$	1
Liquid pool $(\theta \ll 1)$	$\frac{d}{dt}(\gamma h_0 \theta)$	$\eta \left(\frac{\dot{h}_0}{h_0}\right)^2 \frac{h_0^2}{\theta}$	$\frac{\gamma t}{\eta} \theta^2$	1

Table 2: Scaling laws in the inertial regime: $E_\gamma = E_{\text{kin}}$. Cases for which the drop curvature matters invoke $w = r_0^2/R$ as the bridge width, and $\tau_i = \sqrt{\rho R^3/\gamma}$ as the inertial timescale.

	Capillary energy	Kinetic energy	Bridge scaling	Exponent
	$\gamma \Delta \mathcal{A}$	$\rho v^2 \mathcal{V}$	$r_0(t)$	β
Spherical drops	γr_0^2	$\rho \dot{r}_0^2 r_0^2 w$	$\left(\frac{t}{\tau_i}\right)^{1/2} R$	1/2
Spherical bubbles	γr_0^2	$\rho \dot{r}_0^2 r_0^2 w$	$\left(\frac{t}{\tau_i}\right)^{1/2} R$	1/2
Conical drops	γr_0^2	$\rho \dot{r}_0^2 r_0^3$	$\left(\frac{\gamma t^2}{\rho}\right)^{1/3}$	2/3
Sessile drops (side view, 2D)	$\gamma \Delta \mathcal{L}$	$\rho v^2 \mathcal{A}$	$h_0(t)$	β
Substrate $(\theta < 90°)$	γh_0	$\rho \dot{h}_0^2 h_0^2$	$\left(\frac{\gamma t^2}{\rho}\right)^{1/3}$	2/3
Substrate $(\theta = 90°)$	γh_0	$\rho \dot{h}_0^2 h_0 w$	$\left(\frac{t}{\tau_i}\right)^{1/2} R$	1/2
Liquid pool $(\theta \ll 1)$	$\gamma h_0 \theta$	$\rho \left(\frac{\dot{h}_0}{\theta}\right)^2 \frac{h_0^2}{\theta}$	$\left(\frac{\gamma t^2 \theta^4}{\rho}\right)^{1/3}$	2/3

$\lambda = \eta/\eta_o$: viscosity ratio relative to outer atmosphere

ρ_o/ρ: density ratio, neglected throughout for droplet coalescence

does not capture logarithmic corrections of the actual viscous coalescence dynamics, which goes like $r_0 \sim t \ln t$. Such corrections call for a more detailed approach beyond the simplified scaling analysis (Sec. 3.1).

2.2.2. Experiments. The first experiments to study the asymptotics of drop coalescence found reasonable agreement with the expected scaling in the low viscosity (Menchaca-Rocha et al. 2001, Wu et al. 2004, Aarts et al. 2005) and high viscosity (Yao et al. 2005) limits. Even if the temporal resolution is high, the main obstacle is the ability to look into the gap of width w between the drops. As a result, the optical method is typically limited to measuring w down to a few microns, which typically involves r_0 down to 50μm, and thus $r_0/R \gtrsim 0.05$, making it difficult to access the asymptotic behavior as $r_0 \to 0$.

To improve on this, an electrical method was developed (Case & Nagel 2008, Paulsen 2013), which relies on measuring the impedance of the entire coalescence cell, comparing it to an electrostatic calculation based on two hemispheres joined by a neck of radius r_0. The
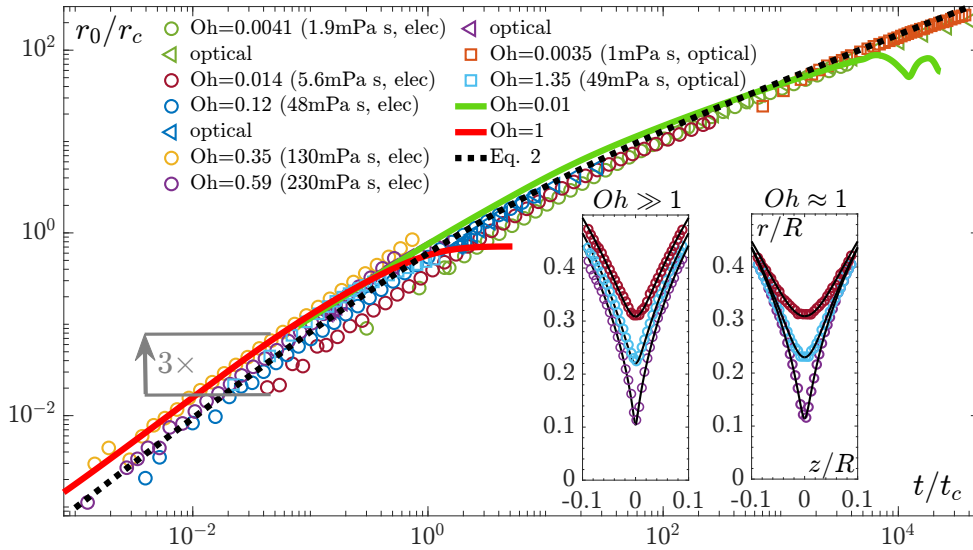
Figure 2: Scaling plot of available data for spherical drop coalescence, comparing experimental data (symbols) and numerical calculations replotted from Sprittles & Shikhmurzaev (2014b) (solid lines), taking η_{air} =0.018 mPa s (corresponding to $\lambda = 2.2 \cdot 10^4 Oh$ for the water-glyercol mixtures considered here). Data are scaled using the crossover scales $r_c = ROh$ and $t_c = \tau_v Oh$, which dictate the crossover from viscous ($t \ll t_c$) to inertial dynamics ($t \gg t_c$). All data are for water-glycerol drops in the presence of air. Circles/triangle are from Paulsen (2013) for electrical/optical and squares are from Thoroddsen et al. (2005b). These data sets were chosen as they use electrical triggers to define accurately the initial contact time. Data from Paulsen (2013) was chosen either (i) as optical and electrical data was available or (ii) to fill in empty regions of the plot. Dashed line represents the empirical crossover function (2) that interpolates between the viscous and inertial regimes. The spread in the experimental data for r_0 is up to a factor of 3. Inset: Experimentally recorded neck shapes (symbols) for two different viscosities in air at $Oh = 370$ and $Oh = 0.62$ from Paulsen (2013), compared to numerical simulations at Oh = ∞ (Stokes) and Oh = 1, respectively. The numerical profiles from Sprittles & Shikhmurzaev (2014b) have been selected for the minimum radius to match at the earliest instance.

resulting values of r_0 were found to be insensitive to the modelling of the neck, and agreed very well with optical measurements in the region of overlap. The electrical method allows to track r_0 down to time scales of 100 ns, so that r_0 is measured down to a radius of $1\mu m$, an improvement of two orders of magnitude.

Following Paulsen et al. (2011), Paulsen (2013), Xia et al. (2019), in Figure 2 experimental data (symbols) have been rescaled using the crossover radius $r_c = ROh$ and crossover time $t_c = \tau_v Oh$, which provides a useful collapse of experimental data over a wide range of Oh. The experiments agree with numerical data obtained from solving the Navier-Stokes equations, including the effect of the surrounding air (red and green solid lines). As will be discussed in more detail in Section 3.1.1 below, these numerical data confirm the presence of logarithmic corrections in the viscous regime, and fall within the experimental scatter, which is up to a factor of 3. Finally, the profiles observed in numerical simulations are in

excellent agreement with those obtained experimentally in the optically accessible range (Figure 2, inset). We thus conclude that simulations, accounting for the influence of the outer air, give a consistent description of the available experimental data.

2.2.3. Crossover. Dimensional analysis shows that the minimum bridge radius can be written in the form $r_0 = R\bar{f}(t/\tau_v, \mathrm{Oh}, \lambda)$, where $\lambda = \eta/\eta_o$ is the viscosity ratio; a small outer density is found to have a vanishing effect on the dynamics. However, we will see in Sec. 3.3 below, that even a small outer viscosity (large λ) changes the structure of the narrow gap between the spheres significantly. Figure 2 shows (dashed line) that the dependence on the remaining parameters τ_v and Oh can be collapsed in a crossover function of a single variable (Paulsen et al. 2011)

$$\frac{r_0}{r_c} = f(\xi) = \left[\frac{1}{C_v \xi} + \frac{1}{C_i \sqrt{\xi}}\right]^{-1}, \quad \text{with} \quad \xi = t/t_c, \qquad\qquad 2.$$

that interpolates between the viscous scaling $r_0/R = C_v t/\tau_v$ and the inertial scaling $r_0/R = C_i\sqrt{t/\tau_i}$. In the plot we used the empirical values $C_v = 1$ and $C_i = 1.5$. Even though the rescaling of data is very good, we emphasize that the collapse in Figure 2 must be considered approximate: a universal crossover function does not exist even for $\lambda = \infty$, owing to logarithmic corrections to the viscous regime (Section 3.1).

2.2.4. Bubbles. The geometry of bubble coalescence superficially resembles that of spherical drops, but the liquid is now confined to a thin sheet on the exterior of the spheres. This sheet is the only portion of the liquid to be set in motion, as the liquid film retracts under the influence of surface tension; the Ohnesorge number Oh_o below now refers to the viscosity η_o of the outer fluid alone. Perhaps surprisingly, the bridge radius now scales as $r_0 \sim t^{1/2}$ for both the viscous and inertial regimes (Paulsen et al. 2014, Munro et al. 2015). The resulting dynamics can therefore be captured by the form

$$\frac{r}{R} = C(\mathrm{Oh}_o)\left(\frac{t}{\tau_i}\right)^{1/2}, \qquad\qquad 3.$$

where $C(\mathrm{Oh}_o)$ is a dimensionless prefactor that accounts for the slowing down upon increasing viscosity. Experimental data (Paulsen et al. 2014) for the prefactor is plotted on Figure 3(a), together with model predictions obtained from direct simulations and from a similarity analysis based on a thin film approximation (Munro et al. 2015).

The retraction of the film separating the bubbles comes with a release of capillary energy $E_\gamma \sim \gamma r_0^2$. At low viscosity, this retraction results in the sheet fluid of volume $\sim r_0^2 w \sim r_0^4/R$ being collected into a growing annular rim of volume $\mathcal{V} \sim r_0^4/R$. The scaling laws for both E_γ and E_{kin} therefore turn out identical to that of drop coalescence, and the same scaling $r_0 \sim t^{1/2}$ ensues in the inertial regime. In the specific case of $\mathrm{Oh}_o = 0$, the original arguments of Taylor (1959) and Culick (1960) can be turned into an exact result, invoking momentum conservation (Keller 1983). During coalescence, the fluid up to a certain radius r_0 is collected inside a rim, which from the shape $z = r^2/(2R)$ of the unperturbed sheet gives a volume $\mathcal{V}_{\mathrm{rim}} = \pi r_0^4/(2R)$. Since the force on the rim exerted by the surface tension per unit length is 2γ, Newton's equation now reads $4\pi\gamma r_0 = d\left(\mathcal{V}_{\mathrm{rim}}\dot{r}_0\right)/dt$, the solution of which yields 3. with $C = (32/3)^{1/4} \approx 1.81$. The same numerical value was found solving similarity equations based on this thin sheet approximation (Munro et al. 2015). The experimental value for the prefactor is slightly lower: $C \approx 1.4$ (Paulsen et al. 2014). The mismatch has

Numerical methods

Until relatively recently, numerical methods have been unable to confirm many of the theoretical predictions for coalescence. This is because they have either (i) captured the global shape of the droplets, without resolving small scales of bridge growth (i.e. neglecting $r_0/R \ll 1$), or (ii) have focused, or 'zoomed in', on the early growth, often in specific flow regimes, without being able to simulate the entire drop's motion (i.e. considering only $r_0/R \ll 1$).

For (i), numerical simulations are able to reproduce coalescing drop shapes and can often recover inviscid (Menchaca-Rocha et al. 2001, Baroudi et al. 2014) and viscous (Baroudi et al. 2016) scalings – these are often based on interface capturing schemes (marker-and-cell, volume of fluid, lattice Boltzmann, etc). For (ii) boundary integral methods have been deployed to compute both inviscid and viscous limits near the bridge front. Here, in the inviscid case, the absence of an outer fluid causes the free surface to overturn and entraps toroidal bubbles (Oguz & Prosperetti 1989, Duchemin et al. 2003). However, whilst some experimental evidence for entrapment has been given (Aryafar & Kavehpour 2008, Fezzaa & Wang 2008) simulations suggest that tiny amounts of outer fluid can prevent the formation of bubbles Sprittles & Shikhmurzaev (2014b) and lead instead to the formation of pockets of gas (also often referred to as 'bubbles'), in front of the evolving neck, as also seen in the viscous case (Eggers et al. 1999).

Considering first a drop in a vacuum, in the viscous regime the smallest length scale is the bridge's radius of curvature $\sim r_0^3/R^2$. Then, for a mm-sized drop, when $r_0 \sim \mu m$ the ratio of minimum length scale to drop size $\sim (r_0/R)^3$ is $\sim 10^{-9}$. Then, for example, to capture this scale with ten volume of fluid (VoF) cells one needs to reach 'level' 30 (as $1/2^{30} \approx 10^{-10}$), well beyond current capabilities. Consequently, most of the simulations probing the earliest stages of coalescence have been performed by interface tracking methods, specifically arbitrary Lagrangian Eulerian finite element (ALE-FEM) codes, that can be tailored to resolve singular dynamics, see the review in Anthony et al. (2023).

For ALE-FEM, one has to initiate the simulation with initial conditions on the velocity profile with a drop shape that creates a finite sized bridge $r_{0,IC}$. The work with ALE-FEM codes began in a series of articles (Sprittles & Shikhmurzaev 2012, 2014b,a), initially focused on forming interfaces, where the effect of the outer fluid is also accounted for. More recently, in Anthony et al. (2020), even smaller scales have been reached in the single-fluid problem. To test both theories proposed in the literature, as well as to compare to experiments, typically one needs $r_{0,IC}/R = 10^{-4}$ to give a few decades of reliable comparison (to satisfy $r_0 > 10 r_{0,IC}$ and $r_0/R \ll 1$). For drop-in-gas, the smallest scale is at most the bridge width, alleviating somewhat the requirements on the grid - for the example above we would now 'only' need level 23! These articles (Sprittles & Shikhmurzaev 2014b, Anthony et al. 2020) established that the initial conditions used in the computation can have a profound influence on the scalings observed, with either under-resolved computation or an offset in the initial conditions potentially leading to different (incorrect) scalings.

been attributed to the (optical) experiment not being able to access the asymptotic regime (Anthony et al. 2017); this is consistent with the absence of a visible rim in experiments (Oratis et al. 2023).

In the viscous regime, bubble coalescence is very different from drop coalescence, since now the flow is confined to the liquid film between the spheres. The relevant volume for dissipation occurs is $\mathcal{V} \sim r_0^4/R$ (rather than r_0^3 for drops), yielding bridge dynamics $r_0 \sim t^{1/2}$ (rather than $t \ln t$ for drops). Similarity analysis for the full range of Oh_o is possible, which in the viscous regime reduces to $C = 0.8909/\sqrt{Oh_o}$ (Munro et al. 2015), in line with the
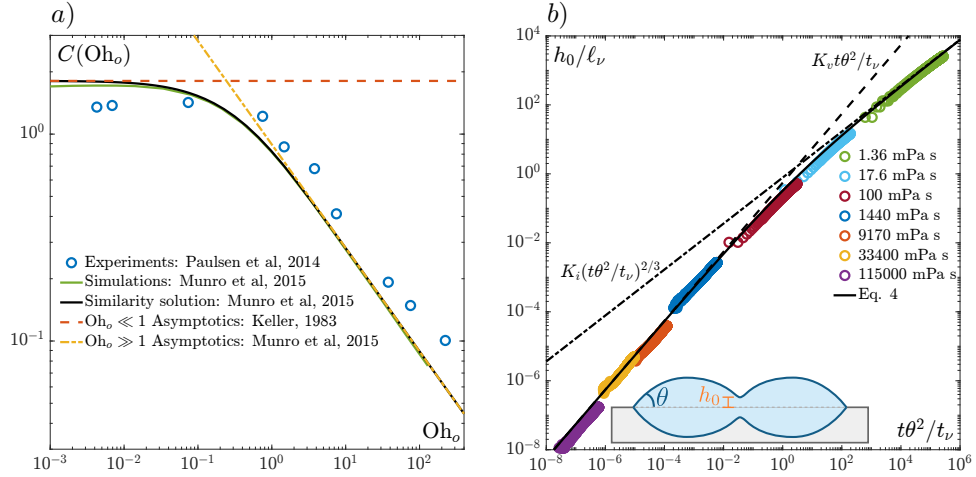
Figure 3: Two examples of viscous to inertial crossover. (a) For spherical bubbles, the bridge dynamics follows $r_0 \sim t^{1/2}$ in both the viscous and inertial regime. The crossover shows up in the prefactor $C(\mathrm{Oh}_o)$ as defined by 3., which is plotted as a function of Oh_o. Experimental measurements (symbols, Paulsen et al. (2014)), numerical simulations (green line), similarity solutions (black line), viscous asymptote (yellow) (Munro et al. 2015), inertial asymptote (red) (Keller 1983). (b) Liquid lenses present a case of geometrically similar coalescence: the side view bridge height h_0 crosses over as time evolves, from $h_0 \sim t$ (viscous) to $h_0 \sim t^{2/3}$ (inertial). Experiments (symbols), crossover function 4. (solid line), viscous asymptote (dash-dotted line, $K_v = 0.552$), inertial asymptote (dashed line, $K_i = 0.781$) (Hack et al. 2020).

experimental trend.

2.3. Geometrically similar initial conditions

Coalescence exponents are not universal, but depend on the fluid geometry upon contact. However, some degree of universality is recovered in the special case of geometrically similar initial conditions. This refers to geometries that are invariant under an isotropic rescaling of all spatial coordinates. Prototypical examples are wedges (Miksis & Vanden-Broeck 1999, Keller et al. 2000, Billingham & King 2005) and cones (Bartlett et al. 2015), for which scales in orthogonal directions are related by an angle. For geometrically similar coalescence, the only relevant scale is the local size of the bridge, and the global drop size R plays no role during the initial stages. Inspecting 1., the independence of R implies an exponent $\alpha = 1$ for viscous coalescence and $\beta = 2/3$ for inertial dynamics. Below we report experiments that fall into this class of geometrically similar coalescence.

2.3.1. Spherical drops with conical tips. Charged drops in a strong electric field can lose their rounded shapes and develop conical tips, similar to Taylor cones (de la Mora 2007). When two charged drops are in close vicinity, the geometry prior to coalescence is thus not necessarily given by a rounded interface, but can consist of cones with a well-defined cone angle θ (Figure 1(iii)). An interesting feature is that conical drops only merge for angles

above a critical value θ_c (Bird et al. 2009). For smaller cone angles, a connecting bridge would actually pinch rather than merge. Assuming inviscid dynamics, the critical angle $\theta_c = 65.3°$ was determined from similarity solutions (Bartlett et al. 2015), consistent with experiment.

Once coalescence occurs in the inertial regime, the minimum bridge radius evolves according to $r_0 \sim (\gamma/\rho)^{1/3} t^{2/3}$, independently of the global size of the drop R (Bird et al. 2009). The independence of the drop size is due to the geometrically similar conical shape: the height and the width of the bridge are both proportional to r_0, the two scales being related by the cone angle. The exponent 2/3 follows on dimensional grounds. Likewise, if viscosity is dominant, dimensional analysis without invoking R yields $r \sim \gamma t/\eta$.

2.3.2. Sessile drops. In many circumstances drops are in contact with a substrate (condensation, rain on a windshield, spraying, printing, etc.), giving rise to slowly spreading or stationary sessile drops. The geometry of such drops consists of a spherical cap (or of a puddle, in case gravity is important (de Gennes et al. 2003)), which makes a well-defined contact angle θ with the substrate, see Fig. 1(iv). Another case of sessile drops are droplets that are floating on a liquid pool, see Fig. 1(v) (de Gennes et al. 2003, Burton & Taborek 2007). A prototypical example of these so-called liquid lenses are the fatty drops floating in a bowl of soup. The geometry of a liquid lens resembles that of a drop on a substrate, but now consists of two spherical caps: one cap above and one cap below the surface of the liquid pool.

In contrast to spherical drops, the geometry of sessile drops does not exhibit axisymmetry. Despite the intricate geometry, when viewed from the side the problem resembles that of two wedges of fluid, of angle θ, which are gently brought into contact (cf. inset of Fig. 3(b), also for the definition of the bridge height h_0). As for conical drops, such wedges fall in the class of geometrically similar coalescence, for which the drop size has no effect on the initial dynamics of the bridge height. Hence, the bridge height $h_0 \sim t$ in the viscous regime (Narhe et al. 2008, Hernandez-Sanchez et al. 2012, Kaneelil et al. 2022, Hack et al. 2020, Klopp & Eremin 2020, Klopp et al. 2020, Scheel et al. 2023), while the inertial limit gives $h_0 \sim t^{2/3}$ (Eddi et al. 2013, Sui et al. 2013, Hack et al. 2020), both for sessile drops and for liquid lenses. Figure 3(b) shows experimental data for liquid lenses, crossing over from the viscous to the inertial asymptotes. The data is accurately described by an empirical crossover function (Hack et al. 2020)

$$\frac{h_0}{\ell_\nu} = f(\xi) = \left[\frac{1}{K_v \xi} + \frac{1}{K_i \xi^{2/3}} \right]^{-1}, \quad \text{with} \quad \xi = \theta^2 t/t_\nu, \qquad 4.$$

with prefactors $K_v = 0.552$ and $K_i = 0.781$, computed from similarity analysis of the thin sheet equations. The crossover only involves intrinsic scales ℓ_ν and t_ν, reflecting the absence of any external scale for geometrically similar coalescence (in constrast to 2.). Importantly, the dependence of $h_0(t)$ on the contact angle θ is different for drops on a substrate and drops on a pool, owing to the different boundary condition. The scalings in Tables 1 and 2 are obtained by a refined version of the analysis presented in Section 4, where we do full justice to the three-dimensional aspects of sessile drop coalescence.

2.4. Other cases

2.4.1. Drops in Hele-Shaw flow.
A Hele-Shaw flow consists of a viscous fluid confined between two closely spaced parallel plates (spacing D, cf. Fig. 1(vi)). During drop coalescence in a Hele-Shaw cell, there is a short initial regime where the bridge radius $r_0 \ll D$, in which case the confinement does not affect the viscous (linear) bridge scaling. However, quickly one approaches a new regime in which $r_0 \gg D$, so that the flow becomes quasi-two-dimensional (Yokota & Okumura 2011). In this regime, the released capillary energy becomes $E_\gamma \sim \gamma D r_0$. The shear rate between the plates $\dot\epsilon \sim \dot r_0/D$, while the relevant volume $\mathcal{V} \sim r_0 D w$. The power balance then gives $r_0 \sim t^{1/4}$, as observed experimentally.

2.4.2. Non-Newtonian fluids.
As illustrated in Fig. 1(vii), the Laplace pressure jump is enhanced in polymeric drops due to strong polymer stretching inside the bridge, where deformation rates are large compared to the polymer relaxation time. As a result, coalescing water-based polymeric drops exhibit bridge curvatures that are much larger than those of pure water drops (Dekker et al. 2022, Bouillant et al. 2022). Yet, the bridge dynamic $r_0(t)$ was found to be identical to that of pure water drops (Dekker et al. 2022) and bubbles (Oratis et al. 2023): polymer stretching remains initially confined to a small sub-region of the bridge, which, even at relatively high polymer concentration, makes their effect too weak to alter the inertial scaling $r_0(t) \sim t^{1/2}$. A polymer-induced slowing down is observed only at slightly later times, with a smaller effective exponent reported for a variety of polymer solutions (Varma et al. 2020). For sessile drops at high concentrations (beyond the dilute regime), such slowing down was observed already for early times (Varma et al. 2021, 2022, Dekker et al. 2022). Other studies involving complex fluids considered how yield stress leads to arrested drop merging (Kern et al. 2022), the effect of shear-thinning on the tip-structure for bubbles coalescence (Kamat et al. 2020), or coalescence of thin liquid crystal domains (Delabre & Cazabat 2010, Klopp et al. 2024). Shear-thinning sessile drops (Chen et al. 2022) are discussed below.

2.5. Different transport mechanisms: A general scaling law for coalescence

Early on, Herring (1950) had proposed a unifying framework to understand sintering by various mechanisms for (non-inertial) material transport, depending on the material and on temperature. For example, at lower temperatures the bulk material becomes solid, and atoms can no longer move in it. Instead, transport is dominated by loosely bound atoms moving around the surface, driven by surface tension (cf. Fig. 1(viii)). As a result, the timescale and coalescence exponents are very different from those for viscous flow. Without going into the detailed physics of various possible transport mechanisms, the coalescence dynamics can be deduced from dimensional analysis. For example, in the case of viscous flow, transport is driven by surface tension γ and damped by viscosity η, thus involving a characteristic velocity γ/η and a timescale $\tau_v = R\eta/\gamma$. As another example, in mean curvature flow (covered below) the normal velocity $\sim A\kappa$, where κ is the mean curvature of the interface; such flows thus involve a transport coefficient $[A]=\mathrm{m}^2/\mathrm{s}$, and the associated timescale becomes $\tau = R^2/A$. Generalizing to different modes of (overdamped) transport, the dynamics involves a transport coefficient $[A]=\mathrm{m}^n/\mathrm{s}$, that naturally gives a timescale $\tau_n = R^n/A$. Power-law fluids driven by surface tension also fall in this class, with $n = 1/n_f$.

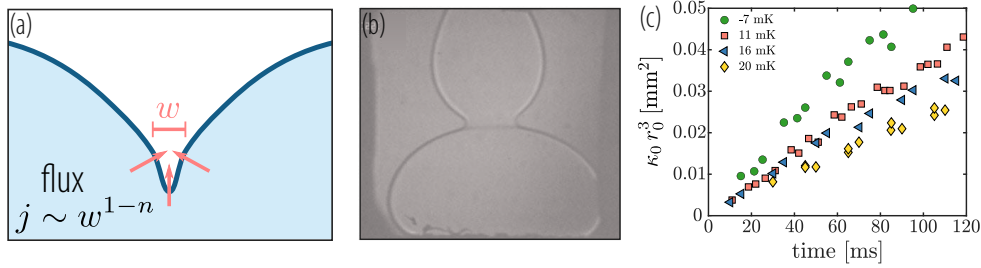n_f: Flow index of a power-law fluid (Newtonian: $n_f = 1$, shear-thinning: $n_f < 1$).

Figure 4: Coalescence beyond viscous transport. (a) The gap of width $w = r_0^2/R$ between two spheres is filled with matter at flux $j \sim w^{1-n}$. Different kinds of transport mechanisms exhibit a different exponent n. (b,c) Mean curvature flow: the flux is proportional to the curvature, $j \sim 1/w$ ($n = 2$). (b) Snapshot during the merging of two ^{3}He crystals, which evolves according to mean curvature flow (Ishiguro et al. 2004). (c) Cube r_0^3 of the bridge radius (normalized by the mean curvature κ_0 of the initial drops), versus time for different temperatures above (red, blue, yellow) and below (green) the minimum of the melting curve. The linear trend implies $r_0 \sim t^{1/3}$, in line with 6. (Ishiguro et al. 2004). Panel (b) adapted with permission from Ishiguro et al. (2004), copyright 2004 American Physical Society.

Applied to coalescence, scaling laws for the initial stages are of the form

$$\frac{r_0}{R} \sim \left(\frac{t}{\tau_n}\right)^\alpha, \quad \text{with} \quad \tau_n = \frac{R^n}{A}. \qquad 5.$$

To find α, we assume the filling of the narrow gap between two spheres is controlled by the single length scale $w = r_0^2/R$ (Herring 1950) (cf. Figure 4(a)). Appealing to the asymptotic equivalence between two-and three dimensional coalescence, the volume flux of material j, which per unit length of the meniscus has dimensions $[j]$=m/s, will be of the form $j \sim Aw^{1-n}$. The gap between the spheres has a (two dimensional) volume $V \sim r_0 w \sim r_0^3/R$, which is thus filled according to $\dot{V} \sim jw \sim Aw^{2-n}$. Solving for $r_0(t)$, one finds the exponent

$$\alpha = \frac{1}{2n-1}. \qquad 6.$$

This new scaling law reproduces the usually accepted exponents for coalescence Kuczynski (1949), Kingery (1960), Eggers et al. (1999). Note that in the viscous case $n = 1$ the coalescence exponent $\alpha = 1$ is often reported wrongly as $1/2$, which can be traced back to the incorrect argument of Frenkel (1945), alluded to in Sec. 2.1.

2.5.1. Mean curvature flow ($n = 2$). Mean curvature flow can be realized by the surface of He^3 crystals close to $T_{\min} = 0.32$ K, where the latent heat vanishes, and melting and freezing is controlled by small differences in chemical potential (Maris 2003, Ishiguro et al. 2004). As a result, the normal velocity is proportional to the mean curvature. Figures 4(b,c) provide an example of merging of He^3 crystals (Ishiguro et al. 2004), which follows $r_0 \sim t^{1/3}$, in line with 6. for $n = 2$. The prefactor can be determined analytically from a detailed calculation of the meniscus shape (Maris 2003).

2.5.2. Sintering by volumetric ($n = 3$) or surface diffusion ($n = 4$). The sintering of metal spheres can be driven by volumetric diffusion of atoms across the bulk, or by the

diffusion of atoms along the surface (Kuczynski 1949, Mullins 1959, Eggers 1998). The former involves a transport coefficient with $n = 3$, while the latter has $n = 4$. According to 6., this gives $r_0 \sim t^{1/5}$ and $r_0 \sim t^{1/7}$, respectively, both of which have been observed experimentally Kuczynski (1949). A closer analysis of merging by surface diffusion, however, reveals that a more subtle argument is needed to derive the growth law (Eggers 1998). The underlying dynamical equation gives rise to surface oscillations: the two sides of the gap between the spheres touches to enclose a void, at which point the dynamics of r_0 restarts. The mechanism of void formation has been used to produce empty structures in silicon (Mizushima et al. 2000).

2.5.3. Other initial conditions. For geometrically similar initial conditions (merging cones) the coalescence dynamics cannot depend on R, which readily implies $\alpha = 1/n$, as is also observed for the blunting of conical tips (Ishiguro et al. 2007, Lamstaes & Eggers 2013). Sessile drop coalescence of power-law fluids is indeed reported to give $\alpha = 1/n = n_f$ (Chen et al. 2022). Another curious case is encountered for the merging of viscous blisters confined between a solid and an elastic sheet; the ratio of bending modulus and viscosity leads to transport with $n = 3$ (Sæter et al. 2024). Unlike cones or spheres, the initial gap between the blisters is very wide and the dynamics is not governed by a single scale; the growth of the bridge between the blisters is not algebraic, but exponential Sæter et al. (2024).

3. Spherical drops

By far the most detailed studies of coalescence have been devoted to the idealized situation of two spherical drops of Newtonian fluid, starting to coalesce at a point of negligible size. The dynamics is controlled by Oh as a single parameter. We consider the limits of vanishing inertia Oh $= \infty$, and of inviscid flow Oh $= 0$, and assess the effect of an outer fluid.

3.1. Very viscous drops, Oh $= \infty$

Let us assume that the shape of the meniscus is described by a similarity solution (Paulsen 2013, Eggers & Fontelos 2015), whose height is set by r_0, and whose width is set by the width $w = r_0^2/R$ of the spacing between two spheres at that scale:

$$ r = r_0 \bar{R}(\xi) \qquad \text{with} \qquad \xi = \frac{zR}{r_0^2}. \qquad\qquad 7. $$

Here $\bar{R}(\xi)$ is a similarity function to be determined below, which depends on the details of the viscous flow. To make 7. consistent with the shape $r \approx \sqrt{2Rz}$ of two spherical drops which away from the bridge region have not yet been deformed, we have to require that $\bar{R} \approx \sqrt{2\xi}$ for large ξ. Even without knowing $\bar{R}$ explicitly, we can conclude that the inverse curvature at the tip, and therefore its smallest length scale Δ, is $r_{zz}^{-1} = r_0^3/(R^2 \bar{R}'') \sim r_0^3/R^2$ (Eggers et al. 1999).

To find the time dependence of r_0 (Eggers et al. 1999), one can argue that the flow is driven by surface tension forces, which are concentrated in the highly curved neck region, which forms an azimuthal ring of radius r_0, and which produces a force of strength $2\gamma \mathbf{e}_r$ per unit length. On a scale smaller than r_0, the curvature of the ring can be neglected, and the motion is equivalent to the *two-dimensional* dynamics of two merging cylinders, driven by two opposite point forces of strength 2γ. This confirms that the leading order

asymptotics of two and three dimensional coalescence are equivalent, as has been confirmed by numerical simulation (Sprittles & Shikhmurzaev 2014b).

The forcing is opposed by viscous forces, which at a distance r_0 from a two-dimensional point force $F = 2\gamma$ (known as a Stokeslet (Pozrikidis 1992)) produces a velocity $F \ln r_0/(4\pi\eta)$. The forcing is spread out over the local scale $\Delta \sim r_0^3/R^2$ of the tip, and cut off over the scale r_0 of the ring, with the opposite side pulling in the opposite direction. This produces a radial velocity of the meniscus $\dot{r}_0 \approx v_\eta/(2\pi) \ln(r_0/\Delta)$, where $v_\eta = \gamma/\eta$ is the capillary velocity. Integrating this velocity, one finds to logarithmically leading order

$$\dot{r}_0 \approx (v_\eta/\pi) \ln(R/r_0), \quad r_0(t) \approx -\frac{v_\eta t}{\pi} \ln(v_\eta t/R).$$ 8.

Given the asymptotic equivalence (for early times) of two- and three-dimensional coalescence, an alternative approach is to analyse the exact solution (Hopper 1990, Richardson 1992) of two merging cylinders in Stokes flow. Hopper (1990) found a complex mapping between the cylinders' cross section and the unit disk in terms of a rational function with time-dependent coefficients, describing the entire evolution from reconnection to a single merged circle. Analysis of this mapping yields the minimum radius $r_0/R = \sqrt{2}(1-a^2)/\sqrt{1+a^4}$, where the parameter a is shown to vary with time as

$$\frac{t}{\tau_v} = \frac{\pi}{\sqrt{2}} \int_{a^2}^{1} \frac{dp}{p\sqrt{1+p^2}K(p)},$$ 9.

and where $K(p)$ is the complete elliptic integral of the first kind (Gradshteyn & Ryzhik 2014). This result matches with 8. at early times, to logarithmically leading order, and agrees very well numerical simulations of merging spheres and cylinders in the Stokes limit in absence of an outer atmosphere (Sprittles & Shikhmurzaev 2014b), as is shown in Fig. 5(a). Expanding the entire mapping for $a \approx 1$, one finds the similarity profile corresponding to the similarity solution 7. to be (Paulsen 2013)

$$\bar{R}(\xi) = \sqrt{\frac{1}{2} + \sqrt{4\xi^2 + \frac{1}{4}}},$$ 10.

consistent with $\bar{R} \approx \sqrt{2\xi}$ for large arguments (see also Howison et al. (1997) and Gillow (1998) for a derivation using the slenderness of the cusp). Remarkably, 10. is identical to the similarity solutions describing Moore's instability of vortex sheets (de la Hoz et al. 2008, Eggers & Fontelos 2015), and other non-local transport equations (Eggers & Fontelos 2019).

3.1.1. Inertial corrections. Initial experimental and numerical results for $r_0(t)$ led Paulsen et al. (2012) to hypothesise the existence of a new "inertially limited viscous" (ILV) regime, in which inertia would intervene to make $r_0(t)$ linear at early times, regardless of the drop viscosity. Theoretically, this was motivated by the fact that inertialess coalescence (i.e. Oh $= \infty$) described by Hopper's solution (Hopper 1990), drives a uniform translation of both drops by a distance $r_0^2/(4R) = w/4$. This effect is illustrated in Fig. 5(b), showing a horizontal shift of the similarity solution 10. (black dashed line), relative to the original drop position (red dotted line). Estimating drop inertia at finite Oh, it follows that at early times surface tension is not sufficiently strong to move an entire drop by a distance $w/4$; thus, outside the viscous bridge region, the drop remains at its original position, marked by the red dotted line.
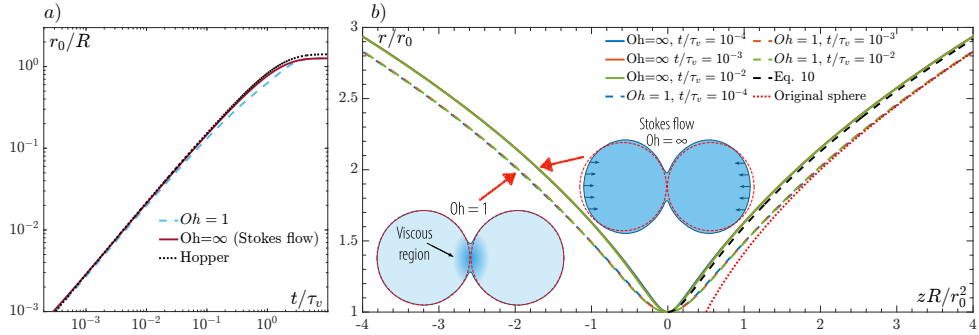
Figure 5: (a) Bridge radius $r_0(t)$ for three-dimensional spherical drop coalescence at Oh $= 1$ and Oh $= \infty$ at early times, compared to 9. (Hopper 1990). (b) Without inertia (Stokes flow) the drop profile near the meniscus collapses for early times onto the similarity solution 10. (black dashed line). For Oh $= 1$ and early times, collapse is on a different similarity solution, which asymptotes to spheres still at their original position (red dotted line). Figures replotted from simulation data presented in Sprittles & Shikhmurzaev (2014b).

But as seen in Fig. 5(a), in reality r_0 remains virtually unaffected by drop translation at early times, in agreement with all recent numerical data (Sprittles & Shikhmurzaev 2014b, Anthony et al. 2023); as a result, r_0 agrees with Hopper's solution, which includes logarithmic corrections (Eggers et al. 1999). In other words the arguments leading to 8. still hold at early times, even at finite Oh: the bridge region remains purely viscous, and there is no ILV regime for $r_0(t)$. However, a closer inspection of the self-similar meniscus region (Fig. 5(b)) shows that a finite Oh-value does change the similarity function $\bar{R}(\xi)$ (cf. 10.), now shown as the green dashed line. Numerical solutions for Oh $= 1$ collapse onto this new similarity profile, which now has to fit onto the un-shifted drop (red dotted line), and thus differs from its Oh $= \infty$ version 10..

3.2. Inviscid drops, Oh $= 0$

In the viscously dominated case, the dynamics were taking place over a wide range of scales, between r_0^3/R^2 and r_0. In the inviscid case, by contrast, the dynamics are local; the only available length scale is the neck width $w = r_0^2/R$. Invoking this length in the energy balance gives the inviscid scaling (Section 2.2),

$$ r_0 = C_i \left(\frac{\gamma R}{\rho} \right)^{1/4} t^{1/2}. \qquad\qquad 11. $$

This result has been obtained by a variety of essentially equivalent arguments (Eggers et al. 1999, Duchemin et al. 2003, Biance et al. 2004), and has been proven robust in many experiments (Wu et al. 2004, Case & Nagel 2008, Paulsen 2013, Chireux et al. 2021) and simulations (Sprittles & Shikhmurzaev 2014a,b). The constant is found to be close to $C_i \approx 1.5$ in experiment (see Fig. 2) and simulations (Sprittles & Shikhmurzaev 2014a), with a slightly higher value of $C_i \approx 1.62$ given in (Paulsen 2013). Once again, the local dynamics are controlled by the large curvature near the tip, much larger than the azimuthal curvature of the liquid bridge connecting the drops (Eggers et al. 1999). Thus coalescence in two and three dimensions lead to the same bridge dynamics in the limit of small r_0.

Practical Challenges, First Contact, & Microscopic Effects

Optical imaging of the initial stages of coalescence is challenging, due to the cusp-like gap into which the experimentalist must search for the first signs that merging has occurred. Furthermore, even when electrical methods are used to signify contact, e.g. in Thoroddsen et al. (2005a) and Paulsen et al. (2011), the mechanism by which contact is established, and thus the initial shapes of the two drops, is unclear.

Throughout the literature, it has been speculated that the intervening air could provide a lubricating cushion that can deform the drops and even prevent contact at the centre. To analyse this effect, experiments in Paulsen (2013) vary U over seven orders of magnitude, going as low as 17 nm/s, and show that for approach speeds $< 3 \times 10^{-4}$ m/s, the crossover between viscous and inertial regimes remains unchanged. Recent simulations, based on the framework in Sprittles (2024), that includes both gas kinetic effects and van der Waals (vdW) forces between the approaching interfaces, support this result, see Deblais et al. (2024). In particular, simulations show a vdW-driven 'jump to contact' that initiates merging of mm-sized drops at a distance $d_{\min}$ of 10's of nanometres, in agreement with experiment (Chireux et al. 2018). The much larger value of $d_{\min} \sim 160$ nm suggested in Paulsen (2013) is likely due to the strong electric field used there. Clearly, the relation between the approach stage and subsequent coalescence is worthy of further experimental and theoretical analysis; the dynamics of the jump-to-contact has been investigated theoretically in more detail by Beaty & Lister (2022, 2023).

On top of these effects, one has thermal fluctuations that for typical fluids drive nanoscale interfacial waves that deform the spherical shape of the drops. For larger drops these can act as initial perturbations that initiate the 'jump to contact' instability whilst for smaller 'nanodrops' they can drive off-centre contacts, see Perumanath et al. (2019), introducing stochasticity into the coalescence process.

A first correction to 11. can be derived by including the azimuthal curvature (Sprittles & Shikhmurzaev 2014a, Xia et al. 2019), which significantly improves the agreement with numerical simulations for $r_0/R \gtrsim 0.1$.

To analytically determine the prefactor C_i of the inviscid scaling, one might be tempted to resort to a similarity analysis as for the viscous case. Experimental profiles indeed exhibit a reasonable collapse (Dekker et al. 2022) when scaling radial and axial scales with r_0 and w, respectively, in line with 7.. However, such a local similarity description only applies in an approximate sense. In Duchemin et al. (2003) inviscid coalescence was analyzed theoretically assuming potential flow, and ignoring the effect of the outer atmosphere. However, the bridge dynamics lead to capillary waves fed by a growing bulbous end, and eventually reconnection (Duchemin et al. 2003, Billingham & King 2005), after a time $\tau_0\sqrt{\rho w^3/\gamma}$, the meniscus having traveled a distance $\Delta_0 w$; the dimensionless constants $\tau_0 = 10$ and $\Delta_0 = 7.6$ were determined numerically. Averaging over many reconnection events (Eggers 1998), one obtains $C_i = \sqrt{2\Delta_0/\tau_0} \approx \sqrt{20/7.6} \approx 1.62$. At the discrete reconnection events, the profile is described approximately by 7.; however, this is not an example of discrete self-similarity (Eggers & Fontelos 2015), since reconnection times do not scale geometrically. The reconnections can be suppressed by including the outer fluid into the description (Sprittles & Shikhmurzaev 2014b). As is discussed below, the presence of an outer fluid also introduces a new length scale in the problem, breaking the similarity form 7..
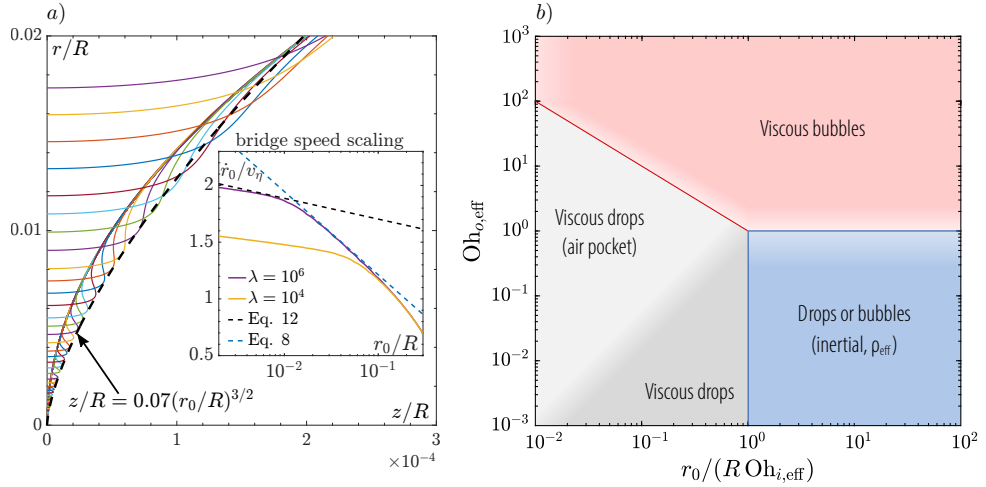
Figure 6: (a) Growth of an air bubble ($\mathrm{Oh} = \infty$, $\lambda = 10^4$) consistent with all outer fluid accumulating at the meniscus; the inset shows the bridge velocity for $\lambda = 10^4$ and 10^6 according to 12. (including the effect of the outer fluid), and 8. (neglecting the outer fluid). This is replotted from simulation data presented in Sprittles & Shikhmurzaev (2014b). (b) Phase map for spherical coalescence in an outer fluid. We defined effective Ohnesorge for the inner and outer fluids, using the effective density $\rho_{\mathrm{eff}} = \rho + \rho_o$. Hence, $\mathrm{Oh}_{i/o,\mathrm{eff}} = \eta_{i/o}/\sqrt{\gamma R \rho_{\mathrm{eff}}}$. The transition in the grey zone is not universal (here sketched for $\mathrm{Oh}_{i,\mathrm{eff}} = 1$).

3.3. An outer fluid

Unavoidably, physical systems involve the presence of an outer fluid, most often a gas atmosphere. This introduces the density ratio ρ/ρ_o, and most importantly the viscosity ratio $\lambda = \eta/\eta_o$ between the inner and outer fluids as additional parameters. Even the smallest external viscosity will lead to a significant change in behavior (Eggers et al. 1999), as the external fluid is trapped inside a very narrow channel between the two drops, from which it cannot escape. As a result, the outer fluid accumulates inside the meniscus region, forming a toroidal bubble, see Fig. 6(a), as has been observed experimentally for drop coalescence in oil (Aryafar & Kavehpour 2008), in air (Deblais et al. 2024), and in numerical simulations (Sprittles & Shikhmurzaev 2014b). The volume of the toroidal bubble follows from integrating over the width of the gap $z = r^2/R$ from 0 to r_0, which gives $\mathcal{V}_b = \pi r_0^4/(2R)$. This leads to a toroidal bubble of radius $r_b \sim r_0^{3/2}/R^{1/2}$, as confirmed in Fig. 6(a).

3.3.1. Viscous drops.
For drops of high viscosity (large Oh) without outer fluid, the dynamics involved the meniscus curvature $\Delta \sim r_0^3/R^2$ as the smallest scale. Due to the presence of the toroidal bubble, the smallest scale is replaced by the bubble size $r_b \sim r_0^{3/2}/R^{1/2}$, changing the dynamics to (Eggers et al. 1999),

$$\dot{r}_0 \approx \frac{v_\eta}{2\pi} \ln(r_0/r_b) \approx \frac{v_\eta}{4\pi} \ln(R/r_0), \quad r_0(t) \approx -\frac{v_\eta t}{4\pi} \ln(v_\eta t/R). \qquad 12.$$

Comparing to 8., this induces a slower dynamics, by a factor 4, compared to viscous coalescence without an outer fluid. The scaling 12. is confirmed numerically (Fig. 6(a), inset), which shows the speed of retraction $\dot{r}_0$ as a function of r_0. Even for a very large viscosity

ratio λ (small external velocity), 12. is observed at early times. The dynamics crosses over to 8. at the later stages, during which the outer fluid escapes and the toroidal bubble disappears. The range of r_0-values for which a toroidal bubble is sustained has been estimated as $r_0/R \lesssim \lambda^{-2/3}$, by comparing the the pressure inside the drop to the lubrication pressure due to the emptying of the bubble inside the drop (Eggers et al. 1999). An analysis of numerical data in Sprittles & Shikhmurzaev (2014b) indicates $r_0/R \lesssim \lambda^{-1/3}$; the origin of this discrepancy is not known.

The above pertains to small external viscosity ($\lambda \gg 1$). The regime where the outer fluid has comparable or large viscosity ($\lambda \lesssim 1$) has been investigated by Paulsen et al. (2014), for which the toroidal bubble gives way to a smoothened profile (Eggers et al. 1999, Munro et al. 2015). Using the results in Table 1 for the idealized cases $\lambda = \infty$ (drops) and $\lambda = 0$ (bubbles), we estimate the relative importance of dissipation in the outer/inner fluid, $P_o/P_i \sim \lambda^{-1} r_0/R$. Hence, crossover between dominance of viscous effects of the inner fluid and dominance of the outer fluid takes place at $r_0/R \sim \lambda = \eta/\eta_o$ (Paulsen et al. 2014).

3.3.2. Inviscid drops. Turning to the case of inertially dominated drops (small Oh), for small r_0/R the lubrication pressure in the air pocket strongly inhibits the reconnection of the two sides of the drops. In addition, even if the drop viscosity is small, the resisting factor is now the fluid inertia, which has to be accelerated by the stress exerted by the gas. One can theoretically exploit the presence of the toroidal bubble, as the configuration is identical to the film retraction encountered during inviscid bubble coalescence described in Section 2.2.4, the only difference being the effective mass $\alpha \rho \mathcal{V}_b$ in the exterior of the toroidal bubble; α is an added mass coefficient (Batchelor 1967), which is unity in the case of a circular bubble in two dimensions. The modified result from Keller (1983) then reads $C_i = (32/(3\alpha))^{1/4} \approx 1.8$, with the inertial timescale τ_i based on the density of the drop. In the two-fluid case, the total mass set into motion reads $\rho_{\text{eff}} \mathcal{V}$, with effective density $\rho_{\text{eff}} \approx \rho + \rho_o$. We therefore propose $r_0/R \sim (t/\tau_{i,\text{eff}})^{1/2}$ as a good approximation for inviscid two-fluid coalescence, with an effective inertial time $\tau_{i,\text{eff}}$ based on ρ_{eff}.

3.3.3. Regime map. The relative roles of inner/outer fluids are summarized in a regime map (Fig. 6(b), modified from Paulsen et al. (2014)). Since the effect of inertia is captured by ρ_{eff}, we define effective Ohnesorge numbers for the inner/outer fluid as $\text{Oh}_{i/o,\text{eff}} = \eta_{i/o}/\sqrt{\gamma R \rho_{\text{eff}}}$. The vertical axis depends on material properties, while the horizontal axis involves the size of the bridge r_0, which grows in time. Irrespective of $\text{Oh}_{o,\text{eff}}$, the asymptotics for $r_0 \to 0$ is always viscous with $r_0 \sim t \ln t$. Initially, the outer fluid collects in an air pocket and the dynamics follows 12.. At small outer viscosity ($\text{Oh}_{o,\text{eff}} \lesssim 1$), the air escapes over time and the dynamics gives way to the Hopper solution 8. (Fig. 6(a)), before crossing over into the inertial regime with $r_0 \sim t^{1/2}$. At large outer viscosity ($\text{Oh}_{o,\text{eff}} \gtrsim 1$), the outer fluid never escapes the pocket and the inertial regime is not reached. Instead, one crosses directly from 12. to the viscous bubble regime $r_0 \sim t^{1/2}$.

4. Sessile drops

Sessile drops on a solid substrate or floating on another liquid take the shape of spherical caps. On a (super)hydrophobic surface, the droplet contact angle $\theta > 90°$, and the initial contact occurs at a finite height above the substrate; the initial dynamics of the small liquid bridge are not influenced by the substrate and follow that of spherical drops (Keij et al.
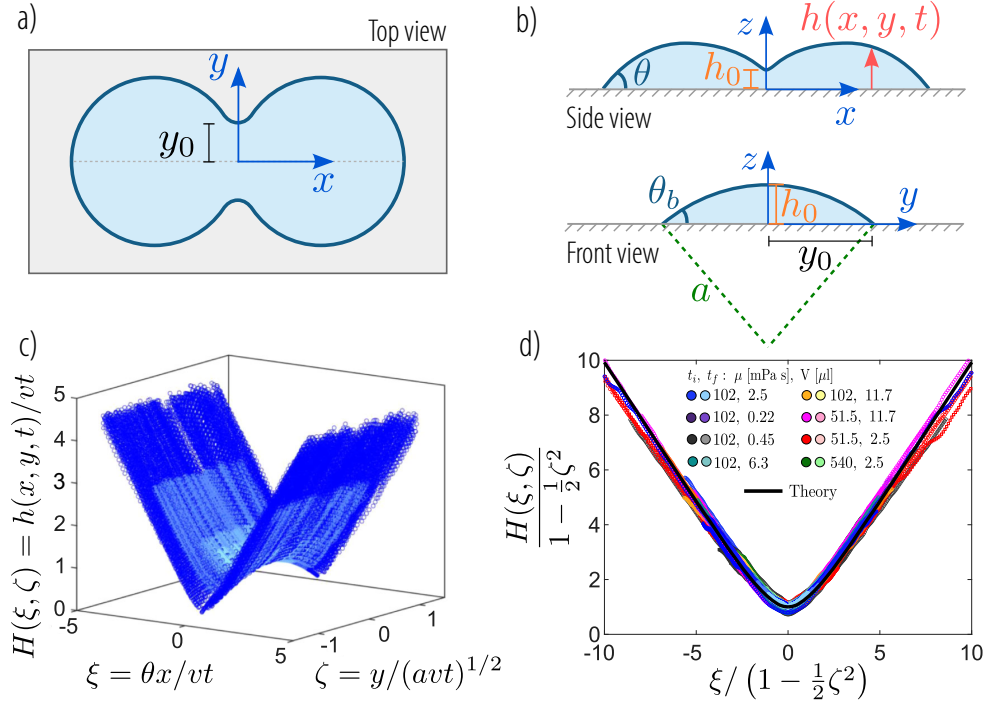
Figure 7: Three-dimensional coalescence of drops on a substrate. Upper panels: schematics representing (a) Top view defining bridge width y_0. (b) Side view defining bridge height h_0 and the contact angle θ; front view, showing the cross-section of the liquid bridge with the bridge angle θ_b and bridge radius of curvature a. Lower panels show experimental profiles of the bridge region during the coalescence of viscous silicone oil drops on a glass substrate (Kaneelil et al. 2022). (c) Collapse of bridge profiles according to the similarity form 14., with constant a. (d) Collapse of data for profiles taken at three different y locations and at multiple times, compared to the theoretical prediction $H^{(1)}$ (solid line) obtained from 15.. Panelc (c,d) adapted with permission from Kaneelil et al. (2022), copyright 2022 American Physical Society.

2013), and the released kinetic energy can even lead to droplet jumping (Thoroddsen & Takehara 2000, Boreyko & Chen 2009). Here we are interested in cases with $\theta \leq 90°$, such that the drop coalescence starts at the substrate. The bridge takes the form of a saddle, described by a function $h(x, y, t)$ (Figure 7). The bridge height $h_0(t)$ and bridge width $y_0(t)$ are defined respectively from the side view and top view perspectives.

As argued in Section 2.3, the bridge height $h_0(t)$ falls in the class of geometrically similar coalescence, which comes with universal exponents $\alpha = 1$ (viscous) and $\alpha = 2/3$ (inertial). However, the geometric relation between top view and side view coalescence of spherical cap-shaped drops is not universal. Following the classification of singularities proposed in Dallaston et al. (2021), we characterize various cases of sessile drop coalescence as "point-like" ($y_0 \sim h_0$), or as "quasi-one-dimensional" ($y_0 \gg h_0$).

4.1. Viscous drops with small contact angles: $\theta \ll 1$

4.1.1. Viscous drops on a substrate. Figure 7(c) shows experimental profiles of the three-dimensional shape of the bridge for two highly viscous silicone oil drops merging on a glass substrate (Kaneelil et al. 2022). At $t = 0$, coalescence starts at the plane of symmetry $y = 0$, according to a linear growth $h(x = 0, y = 0, t) \equiv h_0(t) = vt$. Away from the centerline ($y \neq 0$), the coalescence starts slightly later, at a time $t_0(y)$. Since the bridge is shallow, the cross-section in the (yz)-plane is assumed parabolic (Figure 7(c)), so that $vt_0 = y^2/2a$. Here a is the radius of curvature of the bridge, which relates to the bridge width as $y_0 = (2ah_0)^{1/2}$. In experiments for viscous drops, a was found constant in time and set by the global drop size (Kaneelil et al. 2022). Hence, the bridge width $y_0 \sim t^{1/2}$ (Ristenpart et al. 2006, Narhe et al. 2008), which during the initial stages of coalescence is much larger than the height $h_0 \sim t$. As such, viscous sessile drop coalescence falls in the class of quasi-one-dimensional singularities.

The evolution of $h(x, y, t)$ can be described by two similarity variables: $\xi = x\theta/vt$ in the plane of symmetry, and $\zeta = y/\sqrt{avt}$ in the transversal direction. Figure 7c shows that this rescaling, combined with h/vt, indeed offers a collapse of experimental profiles taken at different times. With this scaling, a solution of the thin film equation (Eggers & Fontelos 2015)

$$\frac{\partial h}{\partial t} + \frac{\gamma}{3\eta} \nabla \cdot \left(h^3 \nabla \nabla^2 h\right) = 0, \qquad\qquad 13.$$

can be written as (Kaneelil et al. 2022)

$$h(x, y, t) = vtH(\xi, \zeta) \equiv vt \left(1 - \frac{1}{2}\zeta^2\right) H^{(1)} \left(\frac{\xi}{1 - \frac{1}{2}\zeta^2}\right). \qquad\qquad 14.$$

This indeed has the form of a quasi-one-dimensional singularity (Dallaston et al. 2021), where $H^{(1)}$ is a solution of the *one-dimensional* similarity equation (Hernandez-Sanchez et al. 2012, Kaneelil et al. 2022):

$$H - \xi H' + \frac{1}{A} \left(H^3 H'''\right)' = 0. \qquad\qquad 15.$$

The delay time of coalescence in the transverse direction ($\zeta \neq 0$) is accounted for by the factors $1 - \frac{1}{2}\zeta^2$. To mimic the experimental scaling in Figure 7, the similarity function was normalized as $H^{(1)}(0) = 1$. This comes at the expense of a constant $A \equiv 3v/(v_\eta\theta^4)$ in 15., which could in fact be scaled out. Its value $A = 0.819$ is determined from the boundary conditions $H'(\infty) = 1$ and $H''(\infty) = 0$ to guarantee matching to the initial drop shape. The solution thus gives the coalescence velocity $v = 0.273v_\eta\theta^4$ (Hernandez-Sanchez et al. 2012), while the shape $H^{(1)}$ is in Fig. 7(d) seen to agree very well with experimental data for various cuts at constant y, rescaled according to 14..

4.1.2. Viscous lenses. Coalescence of drops floating on a liquid pool has been studied using top and side view experiments (Burton & Taborek 2007, Hack et al. 2020), and via lattice Boltzmann simulations (Scheel et al. 2023). Another experimental realization consists of viscous lenses confined in very thin free-standing liquid crystal films (Klopp & Eremin 2020, Klopp et al. 2020), which allows for imaging of the droplet profiles by interference (cf. inset Fig. 8(a)). In the viscous regime, all studies consistently find that $h_0 \sim y_0 \sim t$. The linear scaling of h_0 in the viscous regime was discussed in Fig. 3(b). The fact that y_0 also grows linearly implies that the bridge angle $\theta_b \approx h_0/y_0$ remains approximately

constant during coalescence, as shown from the experimental data in Fig. 8(a) (Klopp et al. 2020). Viscous lens coalescence therefore corresponds to a two-dimensional singularity of the "point-like" type (Dallaston et al. 2021), for which the bridge grows with the same scaling in all directions. This is an important difference with respect to coalescence of viscous drop on a substrate. Another difference seen in the growth velocity for the bridge height: $v = 0.55 v_\eta \theta^2$ for liquid lenses (Hack et al. 2020), instead of $v = 0.273 v_\eta \theta^4$ for drops on a substrate (Hernandez-Sanchez et al. 2012).

4.2. Contact line motion

4.2.1. Top view versus side view. The transverse motion during coalescence of viscous drops on a solid substrate involves rapidly advancing contact lines. At $x = 0$, according to 14. the contact line position is $y_0(t) \approx (2avt)^{1/2}$ (with constant bridge curvature a): the contact line advances at a speed which is formally diverging for $t \to 0$. At the same time, the apparent bridge contact angle θ_b, defined in Fig. 7(c), is $\theta_b \approx \sqrt{2vt/a}$, which goes to zero at initial time $t = 0$. This is a remarkable feature, given that contact lines rapidly advancing over solid surfaces usually lead to an enhancement of the apparent contact angle (compared to the equilibrium angle θ).

We have already seen for viscous drops that the relation between top view and side view is not universal (constant a on a substrate versus constant θ_b for lenses). The inertial regime probed by water drops on a substrate ($\theta \approx 70°$) show both h_0 and y_0 to scale with the inertial exponent 2/3, with $\theta_b \approx \theta$ (Eddi et al. 2013); yet corresponding numerical simulations report an exponent 1/2 for y_0 (Sui et al. 2013). Likewise, experiments (Burton & Taborek 2007) and numerics (Scheel et al. 2023) for inertial lenses report $y_0 \sim t^{1/2}$ (while we recall $h_0 \sim t^{2/3}$). In general, it is not understood when sessile drop coalescence exhibits $y_0 \sim h_0$ (point-like singularity) or $y_0 \gg h_0$ (quasi-one-dimensional singularity).

4.2.2. Hemispherical drops: $\theta = 90°$. A special case arises when $\theta = 90°$, for which the droplets form perfect hemispheres. Figure 8(b) shows experimental results for water drops (inertial regime) showing $h_0(t) \sim t^{1/2}$ (Eddi et al. 2013). Within experimental uncertainty, the data are indistinguishable from $r_0(t)$ obtained for spherical coalescence for which no substrate is present. Hence, the substrate has no measurable effect on the bridge growth. We recall that water drops on a substrate that meet with $\theta < 90°$ exhibit an initial dynamics $h_0 \sim t^{2/3}$. For angles close to (but smaller than) $\theta = 90°$, the 2/3 scaling is observed only over a very short time, quickly crossing over to the 1/2 regime (Sui et al. 2013).

4.2.3. The spreading-coalescence analogy. When a droplet is deposited very gently on a substrate, with negligible impact velocity, a very rapid contact line motion ensues (Figure 8). Interestingly, the dynamics of the contact radius for the initial spreading of water drops follow $r_0 \sim t^{1/2}$ (Biance et al. 2004, Carlson et al. 2011, Winkels et al. 2012, Stapelbroek et al. 2014), and an analogy with inertial coalescence was already suggested by Biance et al. (2004). Figure 8(b) compares directly the liquid bridge dynamics $r_0(t)$ for initial spreading and for coalescence of water drops: the datasets nearly fall on top of one another, the best fits giving prefactors $C_i = 1.5$ (coalescence) and $C_i = 1.2$ (spreading). Once again, the presence of a moving contact line has little effect on the initial dynamics of the bridge, even upon changing the wettability (from $\theta = 0°$ to $115°$) or various types of substrate inhomogeneities (Winkels et al. 2012, Stapelbroek et al. 2014). The spreading-coalescence
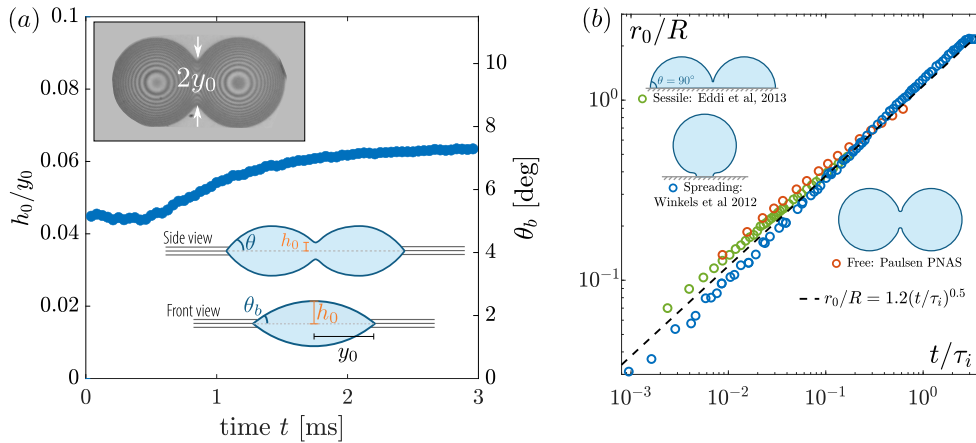
Figure 8: (a) Height-to-width ratio h_0/y_0 during coalescence for viscous lenses, as measured in a free-standing smectic film (Klopp et al. 2020). The ratio remains approximately constant, suggesting a constant bridge angle θ_b. Top left inset courtesy of Christoph Klopp and Ralf Stannarius. (b) Three cases of water drops with identical dynamics for $r_0(t)$: coalescence of hemi-spherical sessile drops ($\theta = 90°$, green, Eddi et al. (2013)), spreading drops (blue, Winkels et al. (2012)), spherical coalescence (red, Paulsen et al. (2012)). Dashed line represents $r_0/R = 1.2(t/\tau_i)^{1/2}$.

analogy is also observed for water drops with (voltage-induced) conical tips: both spreading and coalescence exhibit $r_0 \sim t^{2/3}$ (Courbin et al. 2009).

FUTURE ISSUES

1. The hydrodynamics of just two drops colliding at finite speed is quite complicated, and many aspects remain unexplored (Ashgriz & Poo 1990, Planchette et al. 2012).

2. The numerical data of Fig. 5 suggests the existence of a second similarity solution describing viscous coalescence, but at finite Oh. It remains to discover the mechanism by which inertia comes into play.

3. The observation or prediction of entrapped toroidal bubbles during the coalescence of low viscosity drops remains an intriguing possibility. Whilst conventional lubrication in the gas prevents their formation, it is possible that in narrow gaps kinetic effects reduce the apparent viscosity of the gas and conspire with van der Waals forces, as considered in Sprittles (2024), to entrap a trail of bubbles.

4. How the outer fluid combines with microscopic effects to provide an initial condition for coalescence has only been touched upon (Deblais et al. 2024) and deserves further attention. How are the approach, reconnection and coalescence phases related?

5. For the coalescence of sessile drops, the relation between the bridge height and of the bridge width is not universal, and not understood.

6. What is the effect of contact line motion on coalescence on a substrate? Why does the contact line hardly influence the initial stages of spreading?

DISCLOSURE STATEMENT

ACKNOWLEDGMENTS

LITERATURE CITED

Aarts DGAL, Lekkerkerker HNW, H. Guo G. H. Wegdam DB. 2005. Hydrodynamics of droplet coalescence. *Phys. Rev. Lett.* 95:164503

Anthony CR, Harris MT, Basaran OA. 2020. Initial regime of drop coalescence. *Phys. Rev. Fluids* 5:033608

Anthony CR, Kamat PM, Thete SS, Munro JP, Lister JR, et al. 2017. Scaling laws and dynamics of bubble coalescence. *Phys. Rev. Fluids* 2:083601

Anthony CR, Wee H, Garg V, Thete SS, Kamat PM, et al. 2023. Sharp interface methods for simulation and analysis of free surface flows with singularities: Breakup and coalescence. *Annual Review of Fluid Mechanics* 55

Aryafar H, Kavehpour HP. 2008. Hydrodynamic instabilities of viscous coalescing droplets. *Phys. Rev. E* 78:037302

Ashgriz N, Poo JY. 1990. Coalescence and separation in binary collisions of liquid drops. *J. Fluid Mech.* 221:183

Baroudi L, Kawaji M, Lee T. 2014. Effects of initial conditions on the simulation of inertial coalescence of two drops. *Comput. Math. Appl.* 67:282–289

Baroudi L, Nagel SR, Lee T. 2016. Comment on viscous coalescence of droplets: A lattice Boltzmann study. *Phys. Fluids* 28:079101

Bartlett CT, Généro GA, Bird JC. 2015. Coalescence and break-up of nearly inviscid conical droplets. *J. Fluid Mech.* 763:369–385

Batchelor GK. 1967. An Introduction to Fluid Dynamics. Cambridge University Press, Cambridge

Beaty E, Lister JR. 2022. Nonuniversal self-similarity for jump-to-contact dynamics between viscous drops under van der waals attraction. *Phys. Rev. Lett.* 129:064501

Beaty E, Lister JR. 2023. Inertial and viscous dynamics of jump-to-contact between fluid drops under van der waals attraction. *J. Fluid Mech.* 957:A25

Biance AL, Clanet C, Quéré D. 2004. First steps of the spreading of a liquid droplet. *Phys. Rev. E* 69:016301

Billingham J, King AC. 2005. Surface-tension-driven flow outside a slender wedge with an application to the inviscid coalescence of drops. *J. Fluid Mech.* 533:193–221

Bird JC, Ristenpart WD, Belmonte A, Stone HA. 2009. Critical angle for electrically driven coalescence of two conical droplets. *Phys. Rev. Lett.* 103(16):164502

Boreyko JB, Chen CH. 2009. Self-propelled dropwise condensate on superhydrophobic surfaces. *Phys. Rev. Lett.* 103(18):184501

Bouillant A, Dekker PJ, Hack MA, Snoeijer JH. 2022. Rapid viscoelastic spreading. *Phys. Rev. Fluids* 7(12):123604

Burton JC, Taborek P. 2007. Role of dimensionality and axisymmetry in fluid pinch-off and coalescence. *Phys. Rev. Lett.* 98(22):224502

Caragine CM, Haley SC, Zidovska A. 2018. Surface fluctuations and coalescence of nucleolar droplets in the human cell nucleus. *Phys. Rev. Lett.* 121:148101

Carlson A, Do-Quang M, Amberg G. 2011. Dissipation in rapid dynamic wetting. *Journal of Fluid Mechanics* 682:213–240

Case SC, Nagel SR. 2008. Coalescence in low-viscosity liquids. *Phys. Rev. Lett.* 100:084503

Chan DYC, Klaseboer E, Manic R. 2011. Film drainage and coalescence between deformable drops and bubbles. *Soft Matter* 7:2235

Chen H, Pan X, Nie Q, Ma Q, Fang H, Yin Z. 2022. Probing the coalescence of non-Newtonian droplets on a substrate. *Physics of Fluids* 34(3):032109

Chesters AK. 1991. The modelling of coalescence processes in fluid-liquid dispersions : a review of current understanding. *Chem. Engin. Res. Design* 69:259

Chireux V, Protat M, Risso F, Ondarcuhu T, Tordjeman P. 2018. Jump-to-contact instability: The nanoscale mechanism of droplet coalescence in air. *Phys. Rev. Fluids* 3:102001(R)

Chireux V, Tordjeman P, Risso F. 2021. Bridge expansion after coalescence of two droplets in air: Inertial regime. *Phys. Fluids* 33:06112

Courbin L, Bird JC, Reyssat M, Stone HA. 2009. Dynamics of wetting: from inertial spreading to viscous imbibition. *Journal of Physics: Condensed Matter* 21(46):464127

Culick FEC. 1960. Comments on a ruptured soap film. *J. Appl. Phys.* 31:1128

Dallaston MC, Fontelos MA, Herrada MA, Lopez-Herrera JM, Eggers J. 2021. Regular and complex singularities of the generalized thin film equation in two dimensions. *J. Fluid Mech.* 917:A20

Davis R, Schonberg J, Rallison J. 1989. The lubrication force between two viscous drops. *Phys. Fluids A* 1:77

de Gennes PG, Brochart-Wyart F, Quéré D. 2003. Capillarity and wetting phenomena: Drops, bubbles, pearls, waves. Springer

de la Hoz F, Fontelos MA, Vega L. 2008. The effect of surface tension on the Moore singularity of vortex sheet dynamics. *J. Nonlin. Sci.* 18:463–484

de la Mora JF. 2007. The fluid dynamics of taylor cones. *Annu Rev. Fluid Mech.* 39:217–243

Deblais A, Xie K, Lewin-Jones P, Aarts D, M. A. Herrada JE, et al. 2024. Early stages of drop coalescence. *arXiv:physics/2402.00500*

Dekker PJ, Hack MA, Tewes W, Datt C, Bouillant A, Snoeijer JH. 2022. When elasticity affects drop coalescence. *Phys. Rev. Lett.* 128:028004

Delabre U, Cazabat AM. 2010. Coalescence driven by line tension in thin nematic films. *Phys. Rev. Lett.* 104(22):227801

Duchemin L, Eggers J, Josserand C. 2003. Inviscid coalescence of drops. *J. Fluid Mech.* 487:167

Eddi A, Winkels KG, Snoeijer JH. 2013. Influence of droplet geometry on the coalescence of low viscosity drops. *Phys. Rev. Lett.* 111(14):144502

Eggers J. 1993. Universal pinching of 3D axisymmetric free-surface flow. *Phys. Rev. Lett.* 71:3458–3460

Eggers J. 1997. Nonlinear dynamics and breakup of free-surface flows. *Rev. Mod. Phys.* 69:865–929

Eggers J. 1998. Coalescence of spheres by surface diffusion. *Phys. Rev. Lett.* 80:2634

Eggers J, Fontelos MA. 2015. Singularities: Formation, structure, and propagation. Cambridge University Press, Cambridge

Eggers J, Fontelos MA. 2019. Selection of singular solutions in non-local transport equations. *Nonlinearity* 33:325

Eggers J, Lister JR, Stone HA. 1999. Coalescence of liquid drops. *J. Fluid Mech.* 401:293–310

Eggers J, Villermaux E. 2008. Physics of liquid jets. *Rep. Progr. Phys.* 71:036601

Fezzaa K, Wang Y. 2008. Ultrafast x-ray phase-contrast imaging of the initial coalescence phase of two water droplets. *Phys. Rev. Lett.* 100:104501

Flenner E, Janosi L, Barz B, Neagu A, Forgacs G, Kosztin I. 2012. Kinetic monte carlo and cellular particle dynamics simulations of multicellular systems. *Phys. Rev. E* 85:031907

Frenkel J. 1945. Viscous flow of crystalline bodies under the action of surface tension. *J. Phys. (Moscow)* 9:385

Gillow K. 1998. Codimension-two free boundary problems. Ph.D. thesis, Oxford University

Gradshteyn IS, Ryzhik IM. 2014. Table of integrals series and products. Academic: New York

Grosser S, Lippoldt J, Oswald L, Merkel M, Sussman DM, et al. 2021. Cell and nucleus shape as an indicator of tissue fluidity in carcinoma. *Phys. Rev. X* 11:011033

Hack MA, Tewes W, Xie Q, Datt C, Harth K, et al. 2020. Self-similar liquid lens coalescence. *Phys. Rev. Lett.* 124(19):194502

Hernandez-Sanchez JF, Lubbers LA, Eddi A, Snoeijer JH. 2012. Symmetric and asymmetric coalescence of drops on a substrate. *Phys. Rev. Lett.* 109:104501

Herring C. 1950. Effect of change of scale on sintering phenomena. *J. Appl. Phys.* 21:301

Hopper RW. 1990. Plane Stokes flow driven by capillarity on a free surface. *J. Fluid Mech.* 213:349

Hopper RW. 1991. Plane Stokes flow driven by capillarity on a free surface. part 2. Further developments. *J. Fluid Mech.* 230:355

Howison SD, Morgan JD, Ockendon JR. 1997. A class of codimension-two free boundahttps://www.overleaf.com/project/643ea1ee6b8623d8c88b4be8ry problems. *SIAM Rev.* 39:221–253

Ishiguro R, Graner F, Rolley E, Balibar S. 2004. Coalescence of crystalline drops. *Phys. Rev. Lett.* 93:235301

Ishiguro R, Graner F, Rolley E, Balibar S, Eggers J. 2007. Dripping of a crystal. *Phys. Rev. E* 75:041606

Kamat PM, Anthony CR, Basaran OA. 2020. Bubble coalescence in low-viscosity power-law fluids. *J. Fluid Mech.* 902:A8

Kamp J, Villwock J, Kraume M. 2017. Drop coalescence in technical liquid/liquid applications: a review on experimental techniques and modeling approaches. *Rev. Chem Eng.* 33:1–47

Kaneelil PR, Pahlavan AA, Xue N, Stone HA. 2022. Three-dimensional self-similarity of coalescing viscous drops in the thin-film regime. *Phys. Rev. Lett.* 129(14):144501

Kavehpour HP. 20015. Coalescence of drops. *Annu. Rev. Fluid Mech.* 47:245

Keij DL, Winkels KG, Castelijns H, Riepen M, Snoeijer JH. 2013. Bubble formation during the collision of a sessile drop with a meniscus. *Physics of Fluids* 25(8):082005

Keller JB. 1983. Breaking of liquid films and threads. *Phys. Fluids* 26:3451–3453

Keller JB, Milewski PA, Vanden-Broeck JM. 2000. Merging and wetting driven by surface tension. *European Journal of Mechanics - B/Fluids* 19(4):491–502

Kern VR, Sæter T, Carlson A. 2022. Viscoplastic sessile drop coalescence. *Phys. Rev. Fluids* 7(8):L081601

Kingery WD. 1960. Regelation, surface diffusion, and ice sintering. *J. Appl. Phys.* 31:833

Klopp C, Eremin A. 2020. On droplet coalescence in quasi-two-dimensional fluids. *Langmuir* 36(35):10615–10621PMID: 32787035

Klopp C, Trittel T, Harth K, Stannarius R. 2024. Coalescence of biphasic droplets embedded in free standing smectic a films. *Soft Matter* 20(5):1036–1046

Klopp C, Trittel T, Stannarius R. 2020. Self similarity of liquid droplet coalescence in a quasi-2d free-standing liquid-crystal film. *Soft Matter* 16(19):4607–4614

Kuczynski GC. 1949. Self-diffusion in sintering of metallic particles. *Trans. AIME* 185:169

Lamstaes C, Eggers J. 2013. Blunting of conical tips by surface diffusion. *Phys. Rev. E* 87:062408

Li J. 2016. Macroscopic model for head-on binary droplet collisions in a gaseous medium. *Phys. Rev. Lett.* 117:214502

Liao Y, Lucas D. 2010. A literature review on mechanisms and models for the coalescence process of fluid particles. *Chem. Engin. Sci.* 65:2851

Lohse D. 2022. Fundamental fluid dynamics challenges in inkjet printing. *Annual Review of Fluid Mechanics* 54(1):349–382

Maris HJ. 2003. Analysis of the early stage of coalescence of helium drops. *Phys. Rev. E* 67:0663

Menchaca-Rocha A, Martinez-Davalos A, Nunez R, Popinet S, Zaleski S. 2001. Coalescence of liquid drops by surface tension. *Phys. Rev. E* 63:046309

Miksis MJ, Vanden-Broeck JM. 1999. Self-similar dynamics of a viscous wedge of fluid. *Physics of Fluids* 11(11):3227–3231

Mizushima I, Sato T, Taniguchi S, Tsunashima Y. 2000. Empty-space-in-silicon technique for fabricating a silicon-on-nothing structure. *Appl. Phys. Lett.* 77:3290–3292

Mullins WW. 1959. Flattening of a nearly plane solid surface due to capillarity. *J. Appl. Phys.* 30:77

Munro JP, Anthony CR, Basaran OA, Lister JR. 2015. Thin-sheet flow between coalescing bubbles. *J. Fluid Mech.* 773:R3

Narhe RD, Beysens DA, Pomeau Y. 2008. Dynamic drying in the early-stage coalescence of droplets sitting on a plate. *EPL* 81(46002)

Nichols FA, Mullins WW. 1965. Morphological changes of a surface of revolution due to capillarity-induced surface diffusion. *J. Appl. Phys.* 36:1826

Oguz HN, Prosperetti A. 1989. Surface-tension effects in the contact of liquid surfaces. *Journal of Fluid Mechanics* 203:149–171

Oratis AT, Bertin V, Snoeijer JH. 2023. Coalescence of bubbles in a viscoelastic liquid. *Phys. Rev. Fluids* 8(8):083603

Paulsen JD. 2013. Approach and coalescence of liquid drops in air. *Phys. Rev. E* 88:063010

Paulsen JD, Burton JC, Nagel SR. 2011. Viscous to inertial crossover in liquid drop coalescence. *Phys. Rev. Lett.* 106:114501

Paulsen JD, Burton JC, Nagel SR, Appathurai S, Harris MT, Basaran OA. 2012. The inexorable resistance of inertia determines the initial regime of drop coalescence. *PNAS* 109:6857

Paulsen JD, Carmigniani R, Kannan A, Burton JC, Nagel SR. 2014. Coalescence of bubbles and drops in an outer fluid. *Nat. Commun.* 5:3182

Peregrine DH, Shoker G, Symon A. 1990. The bifurcation of liquid bridges. *J. Fluid Mech.* 212:25

Perumanath S, Borg MK, Chubynsky MV, Sprittles JE, Reese JM. 2019. Droplet coalescence is initiated by thermal motion. *Phys. Rev. Lett.* 122:104501

Planchette C, Lorenceau E, Brenn G. 2012. The onset of fragmentation in binary liquid drop collisions. *J. Fluid Mech.* 702:5

Pokluda O, Bellehumeur CT, Machopoulos J. 1997. Modification of frenkel's model for sintering. *AIChE J.* 43:3253

Popinet S. 2018. Numerical models of surface tension. *Annu. Rev. Fluid Mech.* 50:49–75

Pozrikidis C. 1992. Boundary integral and singularity methods for linearized flow. Cambridge University Press, Cambridge

Quinn DB, Feng J, Stone HA. 2013. Analytical model for the deformation of a fluid-fluid interface beneath an afm probe. *Langmuir* 29:1427

Rahaman MN. 2010. Kinetics and mechanisms of densification. In *Sintering of advanced materials*. Woodhead Publishin, 33–64

Reynolds O. 1881. On the floating of drops on the surface of water depending only on the purity of the surface. *Manchester Literary and Philosophical Society, Proceedings* 21

Richardson S. 1992. Two-dimensional slow viscous flows with time-dependent free boundaries driven by surface tension. *Euro. Jnl. Appl. Math.* 3:193–207

Ristenpart WD, McCalla PM, Roy RV, Stone HA. 2006. Coalescence of spreading droplets on a wettable substrate. *Phys. Rev. Lett.* 97(064501)

Ryu S, Zhang H, Anuta UJ. 2023. A review on the coalescence of confined drops with a focus on scaling laws for the growth of the liquid bridge. *micromachines* 14:2046

Sæter T, Pedersen C, Snoeijer JH, Salez T, Carlson A. 2024. Coalescence of elastic blisters filled with a viscous fluid. *Phys. Rev. Lett.* 132(7):074001

Scheel T, Xie Q, Sega M, Harting J. 2023. Viscous to inertial coalescence of liquid lenses: A lattice boltzmann investigation. *Phys. Rev. Fluids* 8(7):074201

Sprittles JE. 2024. Gas microfilms in droplet dynamics: When do drops bounce? *Annu. Rev. Fluid Mech.* 56:67

Sprittles JE, Shikhmurzaev YD. 2012. Coalescence of liquid drops: Different models versus experiment. *Phys. Fluids* 24:122105

Sprittles JE, Shikhmurzaev YD. 2014a. Dynamics of liquid drops coalescing in the inertial regime. *Phys. Rev. E* 89:063008

Sprittles JE, Shikhmurzaev YD. 2014b. A parametric study of the coalescence of liquid drops in a viscous gas. *J. Fluid Mech.* 753:279–306

Stapelbroek BBJ, Jansen HP, Kooij ES, Snoeijer JH, Eddi A. 2014. Universal spreading of water drops on complex surfaces. *Soft Matter* 10(15):2641–2648

Sui Y, Maglio M, Spelt PDM, Legendre D, Ding H. 2013. Inertial coalescence of droplets on a partially wetting substrate. *Physics of Fluids* 25(10):101701

Taylor GI. 1959. The dynamics of thin sheets of fluid III. Disintegration of fluid sheets. *Proc. R. Soc. Lond.* 253:313–321

Thoroddsen S, Takehara K, Etoh T. 2005a. The coalescence speed of a pendent and a sessile drop. *Journal of Fluid Mechanics* 527:85–114

Thoroddsen ST, Etoh EG, Takeara K. 2008. High-speed imaging of drops and bubbles. *Annu. Rev. Fluid Mech.* 40:257

Thoroddsen ST, Takehara K. 2000. The coalescence cascade of a drop. *Phys. Fluids* 12(6):1265–1267

Thoroddsen ST, Takehara K, Etoh TG. 2005b. The coalescence speed of a pendent and a sessile drop. *J. Fluid Mech.* 527:85

Tryggvason G, Scardovelli R, Zaleski S. 2011. Direct numerical simulations of gas-liquid multiphase flows. Cambridge University Press

Varma SC, Dasgupta D, Kumar A. 2022. Elasticity can affect droplet coalescence. *Physics of Fluids* 34(9):093112

Varma SC, Saha A, Kumar A. 2021. Coalescence of polymeric sessile drops on a partially wettable substrate. *Physics of Fluids* 33(12):123101

Varma SC, Saha A, Mukherjee S, Bandopadhyay A, Kumar A, Chakraborty S. 2020. Universality in coalescence of polymeric fluids. *Soft Matter* 16(48):10921–10927

Verdier C. 2001. The in influence of the viscosity ratio on polymer droplet collision in quiescent blends. *Polymer* 42:6999

Winkels KG, Weijs JH, Eddi A, Snoeijer JH. 2012. Initial spreading of low-viscosity drops on partially wetting surfaces. *Phys. Rev. E* 85(5):055301

Wu M, Cubaud T, Ho CH. 2004. Scaling law in liquid drop coalescence driven by surface tension. *Phys. Fluids* 16:L51

Xia X, He C, Zhang P. 2019. Universality in the viscous-to-inertial coalescence of liquid droplets. *PNAS* 116:23467

Yao W, Maris HJ, Pennington P, Seidel GM. 2005. Coalescence of viscous liquid drops. *Phys. Rev. E* 71:016309

Yokota M, Okumura K. 2011. Dimensional crossover in the coalescence dynamics of viscous drops confined in between two plates. *PNAS* 108:6395–6398